

## High-resolution helium time-of-flight studies of Rayleigh surface-phonon dispersion curves of LiF, NaF, and KCl

G. Brusdeylins, R. Bruce Doak,\* and J. Peter Toennies

*Max-Planck-Institut für Strömungsforschung, Böttlingerstrasse 4-8,*

*D-3400 Göttingen, Federal Republic of Germany*

(Received 22 October 1982)

A molecular-beam apparatus is described in which a cold He beam ( $\approx 20$  meV) of very high velocity resolution ( $\Delta v/v \approx 0.8\%$ ) is scattered from alkali halide single-crystal surfaces. The velocity distribution of the scattered beam is analyzed using time-of-flight (TOF) techniques. The variation of the TOF spectra with target temperature reveals the influence of multiphonon processes, allowing the regime of single-phonon scattering to be experimentally delineated. The inelastic scattering TOF spectra reveal as many as six sharp maxima, most of which can be attributed to creation or annihilation of single Rayleigh-mode surface phonons. Some evidence is also found for interactions with bulk modes at the surface. Phonon frequencies and wave vectors determined from the TOF spectra allow Rayleigh-mode dispersion curves to be measured out to the Brillouin-zone boundary for the (001) face of LiF, NaF, and KCl along the  $\langle 100 \rangle$  azimuth. The measured dispersion curves agree well with theoretical predictions except for LiF, for which the experimental frequencies are about 10% lower at the zone boundary. For KCl possible evidence is found for a "crossing mode" embedded in the bulk continuum bands. Measurements were also made in the  $\langle 110 \rangle$  azimuth for LiF; however, the scattering intensities were observed to be so weak that measurements to the zone boundary were not possible. The inelastic scattering is found to be significantly affected by resonant processes involving bound states of the gas-surface potential well. However, Benedek's mechanism of kinematic focusing is shown to have usually only a minor effect upon the distribution of scattered intensity with polar incident angle under the present experimental conditions. TOF spectra for different azimuthal angles indicate that a similar kinematic focusing effect may be expected in azimuthal angular distributions.

### I. INTRODUCTION

Very little experimental data are available on the dispersion relations of surface phonons despite their importance for understanding the physics of solid surfaces.<sup>1</sup> Surface phonons also play an important role in gas-surface interactions.<sup>2-5</sup> The energy transfer from atoms and molecules to phonons is fundamental to an understanding of accommodation coefficients and adsorption and desorption kinetics, as well as sticking coefficients. These are all important elementary steps in catalysis.

Broadly speaking, two types of modes are present at the surface: bulk modes and true surface modes. The latter are characterized by their spatial localization at the surface; they have wave vectors  $\vec{Q}$  parallel to the surface and their frequencies  $\omega$  appear in a two-dimensional dispersion relation  $\omega(\vec{Q})$  as discrete curves. The bulk phonons are not localized at the surface and have three-dimensional wave vectors  $\vec{q}$

which project out as bands in the two-dimensional plot  $\omega(\vec{Q})$ . The true surface modes may further be classified as microscopic or macroscopic depending upon whether the depth of penetration is independent of or proportional to the phonon wavelength, respectively. Rayleigh waves are the best known example of the macroscopic phonons. At large wavelengths they are nondispersive and their properties are well described by continuum theory. Long-wavelength Rayleigh waves find extensive applications in electroacoustical microelectronic devices because of their small damping, constant velocity, and the accessibility provided by their surface localization.

At wavelengths comparable with lattice dimensions, atomic theories predict a multitude of acoustical and optical surface modes with significant dispersion. The theory of small-wavelength (dispersive) surface phonons has developed along two lines. de Wette and his co-workers<sup>6,7</sup> have solved the

mechanical equations of motion for layered, infinitely extended, two-dimensional slabs. They have calculated phonon dispersion relationships for the alkali halides using a potential model between the ions based on the Kellermann rigid-ion model and the shell model. The slab method has the advantage that the force law can be accurately specified but the disadvantage that intrinsic computer limitations restrict the number of layers in the slab calculation to at most 20 to 30, making it difficult to compute the detailed density of phonon states required for surface scattering calculations.

The second theoretical approach, introduced by Benedek,<sup>8,9</sup> avoids this impasse through use of a Green's-function method. In Benedek's formulation the equivalent of a many-layered ( $\sim 200$ ) slab may be tractably treated, allowing detailed densities of phonon states at the surface to be extracted.

Dispersion curves predicted using the two methods show close agreement. Figure 1 shows the result of the calculation of Benedek<sup>9</sup> made in 1976 for LiF(001). The calculations reveal a Rayleigh mode with a frequency just below the bulk bands and a rich spectrum of additional acoustical and optical surface modes among and within the broad bulk bands indicated by the shaded areas. Depending on the respective polarizations when the surface modes and bulk bands overlap, the surface modes may remain distinguishable or they may couple to the underlying bulk modes, forming resonant sur-

face modes with corresponding maxima in the density of states for a given parallel momentum.

Detailed calculations have been limited largely to the alkali halides. For metal crystals and semiconductors much less is known about their surface-phonon dispersion curves, because of the problems in calculating the force laws. However, a number of promising beginnings have recently been made.<sup>10-14</sup>

The lack of experimental data on surface phonons results from the insuitability of standard bulk-phonon techniques, notably neutron scattering, for investigating surface modes. Neutrons, by virtue of their small scattering cross sections, are not sensitive to the surface. Nevertheless, since the neutron momenta and energies closely match those of the phonons, some effort has gone into adapting neutron scattering experiments to surface studies.<sup>15</sup> Yet, although it finds application in studying physisorbed layers,<sup>16,17</sup> neutron scattering has provided so far only limited information on surface-phonon dispersion relations.

Two other potentially useful probe particles might seem to be photons and electrons. Yet light scattering<sup>18,19</sup> provides only information on very-long-wavelength phonons. Electron scattering<sup>20</sup> has been shown to couple effectively to the optical Fuchs-Kliewer modes of ionic crystals such as ZnO. However, so far it has not been possible to observe the small energy losses (1-10 meV) associated with surface phonons when using the electron energies ( $\sim 100$  eV) required in order to interact with phonons near the Brillouin-zone boundary. The rather deep penetration of such electrons is also a problem. Thus the scattering of atoms, which are sensitive only to the surface and are well matched in energy and momentum to the phonons, appears to be the most promising approach.

There have been extensive attempts to use inelastic atom-surface scattering to measure surface-phonon dispersion relations.<sup>5</sup> Essentially three different approaches have been used. The earlier attempts<sup>21-23</sup> were based on studying structures in the angular distributions in regions away from the specular or diffraction peaks. These experiments provided some data on long-wavelength surface phonons. A second novel approach<sup>24</sup> utilized phonon-coupled selective adsorption (bound-state resonance) to provide a clear signature in the angular distributions for phonon interactions. From a knowledge of the atom-surface bound-state energies, phonon dispersion curves could be extracted. This method has been very recently applied to the He-graphite system.<sup>25</sup> The third and most straightforward method relied on measurement of the velocity distribution of the scattered atoms, either through use of time-of-flight measurements<sup>26-28</sup> or diffractive dispersion

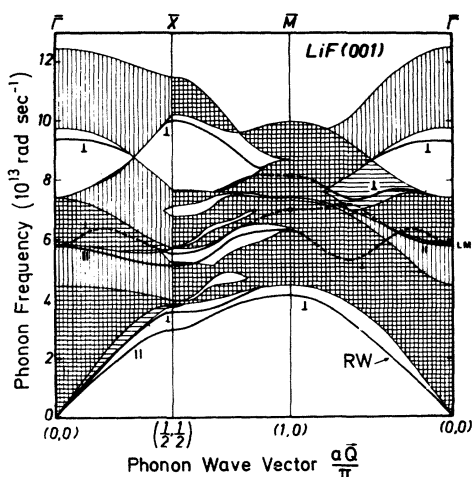


FIG. 1. Surface-phonon dispersion curves of LiF(001) calculated by Benedek (Ref. 9) in 1976 using the breathing-shell model. Localized and resonant surface modes are represented by heavy solid and dashed lines. Resonant surface modes couple to the bulk-phonon bands with the same polarization, which is either sagittal ( $\perp$ ) or parallel ( $\parallel$ ). The Rayleigh mode is indicated by RW. The corresponding irreducible portion of the first Brillouin zone is shown in Fig. 2.

from an analyzer crystal.<sup>29</sup> These previous experiments demonstrated that He atoms interact inelastically with phonons, but were unable to resolve events involving short-wavelength surface waves because of inadequate signal-to-noise levels and too poor a velocity resolution (typically about 10%).

The present paper reports on the results of measurements of time-of-flight distributions of He atomic beams with high angular resolution ( $\Delta\theta_i=0.1^\circ$ ) and with a velocity resolution ( $\Delta v/v \approx 0.8\%$ ) which is roughly an order of magnitude better than in previous work. The dispersion curves  $\omega(\vec{Q})$  are calculated using the conservation of parallel momentum and total energy, assuming only single-phonon interactions,

$$\vec{K}_f = \vec{K}_i + \vec{G} + \vec{Q}, \quad (1a)$$

$$k_f^2 = k_i^2 + \frac{2m\omega(\vec{Q})}{\hbar}, \quad (1b)$$

where throughout capital letters denote vector components in the surface plane,  $\vec{G}$  is a reciprocal-lattice vector,  $\vec{Q}$  is the phonon momentum,  $m$  is the mass of the atom, and  $\omega$  is the phonon frequency. We will refer to positive  $\vec{Q}$  with respect to  $\vec{K}_i$  as *forward* inelastic scattering and negative  $\vec{Q}$  as *backward*. Positive  $\omega$  corresponds to phonon *annihilation* and negative  $\omega$  to phonon *creation*. For in-plane scattering with  $\vec{G}$  and  $\vec{Q}$  in the plane of  $\vec{K}_f$  and  $\vec{K}_i$  we can solve for  $\omega$  and  $\vec{Q}$  by measuring the final scattering angle ( $K_f = k_f \sin\theta_f$ ) and final velocity.

Particular care was taken to improve signal-to-noise ratios by reducing the background He partial pressure at the detector to the lowest possible value. This made it possible to observe interactions with the Rayleigh mode out to the Brillouin-zone boundary and map out the entire dispersion curves for the  $\langle 100 \rangle$  direction of LiF, NaF, and KCl. Part of the dispersion curve for LiF along the  $\langle 110 \rangle$  symmetry directions could also be measured. Figure 2 shows the direct and reciprocal lattices for the alkali halides. The values listed in Fig. 2 are for LiF. The corresponding values for the other crystals can be calculated from the lattice constants. Some important crystal properties for these alkali halides are summarized in Table I. Previously we reported on preliminary measurements on LiF along the  $\langle 100 \rangle$  directions,<sup>30</sup> which were extended out to the zone boundary in a subsequent publication.<sup>31</sup> Some of the work on NaF and KCl has also been reported on briefly previously.<sup>5,32,33</sup> The observation and interpretation of resonant structure in angular distributions between the specular and diffraction peaks has been reported elsewhere.<sup>34</sup>

We begin with a description of the apparatus and estimates of the effective resolution for surface-

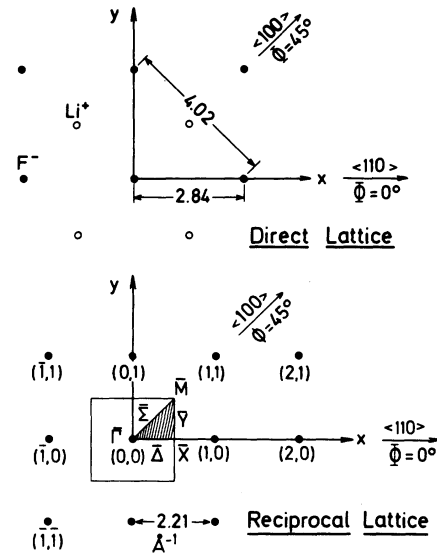


FIG. 2. Two-dimensional lattice of the (001) face of LiF (lattice constants in Å). All crystals studied were of this rock-salt structure. An azimuthal angle of  $0^\circ$  was assigned to the  $\langle 110 \rangle$  direction. Shaded triangle in the lower diagram is the irreducible portion of the first Brillouin zone. Symmetry directions are labeled (Refs. 6 and 7).

mode dispersion curves. The results on time-of-flight distributions at different angles and temperatures are discussed. The energy and momenta of phonons producing the resolved structures are presented in extended-zone diagrams. The measured dispersion relations are then compared with theory. In a concluding section we discuss the observed deviations from theory, the relative role of bulk and surface phonons, and processes which enhance the interaction of atoms with surface phonons.

## II. EXPERIMENTAL ASPECTS

### A. Apparatus

The apparatus consisted of a skimmed-nozzle-beam source, an ultrahigh-vacuum target chamber, and a mass-spectrometer detector. The angle between the incident beam and the outgoing beam was fixed at  $\theta_{SD}=90^\circ$ . Thus the only variable angles were the azimuth of the target crystal (rotation about the surface normal) and its inclination to the incident beam (rotation about an axis perpendicular to both the incident and outgoing beam). As we shall see below this crystal rotation was sufficient to probe the surface-phonon dispersion curves over a wide range of momenta. The monoenergetic primary beam (see below) was pulsed by a rotating-disc

TABLE I. Crystal properties of LiF(001), NaF(001), and KCl(001) surfaces.

Property (at 300 K)	LiF(001)	NaF(001)	KCl(001)
Density ( $10^3 \text{ kg m}^{-3}$ )	2.635	2.558	1.984
Surface lattice constant ( $\text{\AA}$ ) <sup>a</sup>	2.84	3.26	4.45
Melting temperature (K)	1115	1261	1049
Bulk Debye temperature (K) <sup>b</sup>	734	492	235
Surface Debye temperature (K) <sup>c</sup>	350, <sup>d</sup> 610 <sup>e</sup> 415, <sup>f</sup> 513 <sup>e</sup>	411–458 <sup>g</sup> 370, <sup>h</sup> 416 <sup>i</sup>	159 <sup>j</sup>
Wave velocities ( $\text{m sec}^{-1}$ )			
$\langle 100 \rangle$ bulk shear	4910 <sup>k</sup>	3320 <sup>k</sup>	1780 <sup>k</sup>
$\langle 100 \rangle$ surface	3897 <sup>l</sup>	3120 <sup>m</sup>	1753 <sup>l</sup>
$\langle 110 \rangle$ surface	4060 <sup>l</sup>	2650 <sup>o</sup>	1744 <sup>l</sup>
Rayleigh frequency at $\bar{M}$ ( $10^{13} \text{ rad sec}^{-1}$ ) <sup>n</sup>	3.803	2.556	1.01 <sup>p</sup>
Rayleigh frequency at $\bar{X}$ ( $10^{13} \text{ rad sec}^{-1}$ ) <sup>n</sup>	2.986	2.874	1.24 <sup>p</sup>
$\langle 100 \rangle$ surface energy ( $\text{J m}^{-2}$ ) <sup>q</sup>	0.353	0.238	0.131

<sup>a</sup>For a simple cubic lattice.

<sup>b</sup>Reference 35.

<sup>c</sup>Note that these values vary widely depending on whether acceleration into the potential well is included.

<sup>d</sup>Reference 26.

<sup>e</sup>Reference 36.

<sup>f</sup>Reference 37.

<sup>g</sup>Reference 38.

<sup>h</sup>Reference 39.

<sup>i</sup>Reference 40.

<sup>j</sup>Reference 41.

<sup>k</sup>Reference 42.

<sup>l</sup>Reference 43.

<sup>m</sup>Estimated from Fig. 1 of Ref. 44.

<sup>n</sup>Reference 7.

<sup>o</sup>Estimated from Fig. 8 of Ref. 7.

<sup>p</sup>Estimated from Fig. 2 of Ref. 45.

<sup>q</sup>Reference 46.

chopper and collimated before striking the target. The distance from target to detector was roughly 1 m to provide sufficient time-of-flight resolution. Figure 3 shows a schematic diagram of the geometry of the beam-defining slits of the apparatus on a scale in which transverse dimensions have been expanded relative to the longitudinal dimensions by a factor of 100. Since the apparatus has been described in some detail elsewhere<sup>34,47</sup> we repeat here only some of its salient features, the crystal preparation techniques, and—in more detail than previously—the geometrical factors which effect the angular and velocity resolution. Table II summarizes important dimensions, characteristics of the apparatus components, and pressures in the target and detector chambers.

The present apparatus is much improved in velocity resolution compared to previous<sup>21–29</sup> machines. This has been achieved by using highly expanded He

nozzle beams in a manner extensively explored both experimentally<sup>48</sup> and theoretically<sup>49</sup> in this laboratory. It was found that by increasing the stagnation pressure  $p_0$  to 200 atm or more and by using small nozzle holes (in the present case the diameter  $d=5 \mu\text{m}$ ) it was possible to achieve speed ratios in excess of  $S=200$  corresponding to  $\Delta v/v \simeq 1\%$  full width at half maximum (FWHM). With the use of a much smaller nozzle, the gas flow, which is proportional to  $p_0 d^2$ , is only slightly larger than in previous experiments. The present apparatus is equipped with an unbaffled 12 000-l/sec diffusion pump backed by a 500-m<sup>3</sup>/h roots pump to provide a maximum He throughput of about 17 Torr liter/sec. The beam intensity was measured using a pitot-tube stagnation gauge beyond the target (see Fig. 3) to be  $6 \times 10^{19}$  atoms/sr sec.

The long flight time between target and detector was required both to provide adequate time-of-flight

TABLE II. Characteristics of apparatus components.

Source	Orifice diameter, nominal	$5.0 \times 10^{-3}$ mm
	Orifice diameter, from flow measurement	$6-7 \times 10^{-3}$ mm
	Pressure from flow measurement	200 bar
	Temperature	80 K
	He-beam velocity	950 m/sec
	Relative velocity spread (FWHM)	0.008
	Intensity	$6 \times 10^{19}$ atoms/sr sec
Skimmer	Entrance diameter	0.5 mm
	Length: entrance to base	25 mm
	Outside/inside full angles	$32^\circ/25^\circ$
	Orifice-to-skimmer distance	15 mm
Chopper	Double-slit disk, slit diameter	150 mm
	Double-slit disk, slit width	0.25 mm
	Disk rotational frequency ( $\Delta f \leq 0.1\%$ )	150 Hz
	Shutter function (FWHM), nominal	7.5 $\mu$ sec
	Shutter function (FWHM), indicated	4.1 $\mu$ sec
Dimensions	Source-target distance	1.012 m
	Target-detector distance	1.154 m
	Chopper-detector distance	2.014 m
	Fixed-source-target-detector angle	$90.0^\circ$
	Incident-beam full angular spread, nominal	$0.20^\circ$
	Angle subtended by detector from target, nominal	$0.64^\circ$
	Angular resolution, (00) peak, nominal (scanning $\theta_i$ )	$0.19^\circ$
Electronics	EMI 2642/38 18-stage venetian electron multiplier tube	
	ORTEC 9301 preamplifier	
	ORTEC 454 timing filter amplifier	
	MPI in-house buffer/amplifier	
	Tracor-Northern multichannel analyzer, 6.9- $\mu$ sec min channel width	
	Data General Nova 3 computer with CAMAC interface	
Pressures <sup>a</sup>	Target chamber $P_s$ , total pressure	
	Base	$2.6 \times 10^{-9}$ Torr
	Operation, beam chopped	$3.6 \times 10^{-9}$ Torr
	Operation, beam unchopped	$4.6 \times 10^{-8}$ Torr
	Target chamber $P_s$ , He partial pressure	
	Base	$4 \times 10^{-11}$ Torr
	Operation, beam chopped	$2.9 \times 10^{-10}$ Torr
	Operation, beam unchopped	$4.3 \times 10^{-8}$ Torr
	Detector chamber $P_d$ , total pressure	
	Base	$2.8 \times 10^9$ Torr
	Operation	Same
	Detector chamber $P_d$ , He partial pressure	
	Base	$4 \times 10^{-14}$ Torr
Operation, beam chopper	$5 \times 10^{-14}$ Torr	
Operation, beam unchopped	$1.6 \times 10^{-12}$ Torr	

<sup>a</sup>Corrected for ionization-gauge sensitivity for individual gas species with partial pressures determined from residual-gas spectra. Uncorrected ionization gauge readings are roughly a factor of 5 less.

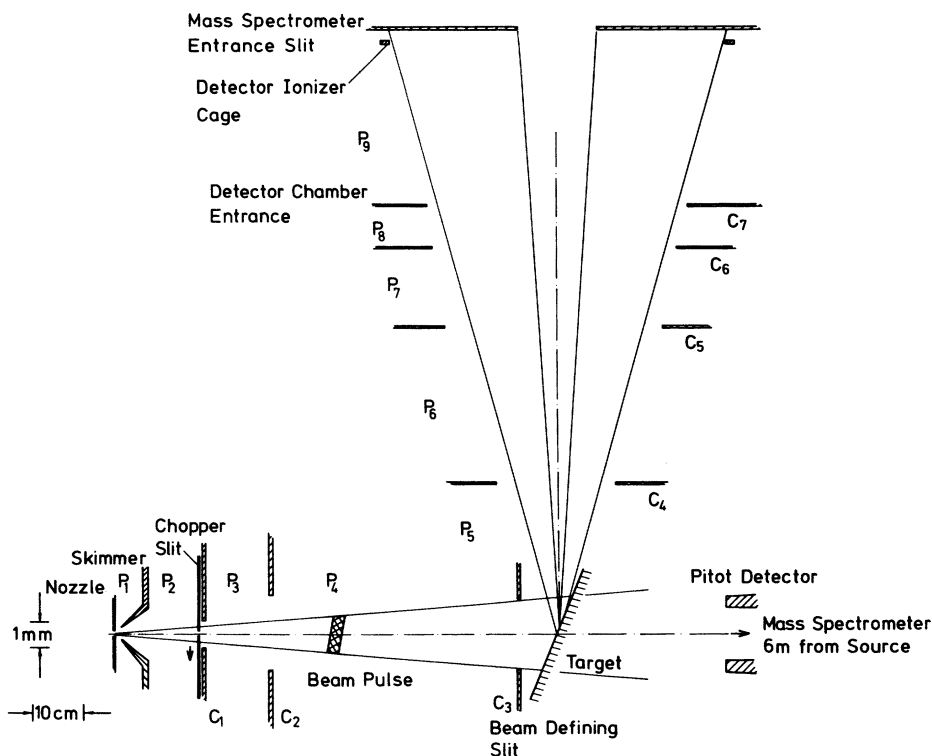


FIG. 3. Beam-defining geometry as employed for the NaF and KCl measurements. Pumping stages ( $P_1$ – $P_9$ ) and collimators ( $C_1$ – $C_7$ ) are labeled.

resolution and to allow three differential pumping stages to be installed between target and detector. Since the beam intensity decreases as the square of the source-detector distance (for a fixed detector size), the effective beam pressure at the detector (estimated to be about  $10^{-13}$  Torr for inelastic scattering) was several orders of magnitude smaller than that obtained with conventional machines. This, however, was more than compensated by the differential pumping which, according to measurements, reduced the helium background by a factor of  $3 \times 10^4$  between target and detector. The background partial pressure of helium in the detector chamber was estimated to be  $5 \times 10^{-14}$  Torr under normal conditions for inelastic time-of-flight measurements.

Oil diffusion pumps were used throughout apart from the target chamber, where a turbopump (Leybold-Heraeus T 450) was used to achieve a base pressure of  $3 \times 10^{-9}$  Torr (without beam and corrected for gas-composition and gauge sensitivity) which rose to about  $4 \times 10^{-9}$  Torr during an inelastic scattering experiment.

The typical integration time for most of the time-of-flight spectra was 1 h, however, for some of

the systems and at certain angles longer integration times (up to 6 h) were required. Angular scans over the entire  $\theta_i$  range between  $20^\circ$  and  $80^\circ$  took also about 1 h.

### B. Target preparation

The LiF, NaF, and KCl single crystals (Korth,<sup>50</sup> Kiel) were all cleaved in air ( $10 \times 7 \times 2$  mm<sup>3</sup>) and then quickly mounted onto the manipulator (Vacuum Generators HPT2 RD2S SM2 LN2 H). All three crystals were cleaned initially and again regularly after several days' operation following a procedure similar to that of Estel *et al.*,<sup>51</sup> by heating to a temperature of about 1000 K for at least 12 h. The presence of sharp diffraction peaks which were all reproducible from one crystal to the next was regarded as evidence for a well-ordered and clean surface. Further evidence for target cleanliness came from *in situ* He scattering studies from LiF in the presence of large doses ( $10^5$  langmuirs) of Ar, H<sub>2</sub>O, and C<sub>2</sub>H<sub>5</sub>OH. (1 langmuir = 1 L =  $10^{-6}$  Torr sec.) For LiF at room temperature this had no effect on either the elastic or inelastic scattering. Only near

liquid-nitrogen temperatures did  $C_2H_5OH$  lead to a reduction in the signals and a broad diffuse background, indicating adsorption onto the LiF surface.

For NaF a new diffraction structure corresponding to an overlayer with double and fourfold lattice spacing was observed when the crystal was cooled to about 120 K in the ambient vacuum.<sup>47</sup> A residual-gas analysis of the ambient vacuum typical to all inelastic scattering experiments revealed the following composition (in Torr):  $H_2$ ,  $2.9 \times 10^{-9}$ ; He,  $2.9 \times 10^{-10}$ ;  $H_2O$ ,  $3.2 \times 10^{-10}$ ;  $N_2/CO$ ,  $4.5 \times 10^{-11}$ ;  $CO_2$ ,  $1.7 \times 10^{-11}$ —at a total pressure of  $3.6 \times 10^{-9}$  Torr. For both LiF and NaF, the adsorption-induced changes in scattered intensity disappeared when the target temperature was raised above the critical adsorption value. This indicated that the adsorption process was reversible. The inelastic scattering features of the angular distribution to be discussed in Sec. III A were found to be particularly sensitive indicators of adsorption, disappearing almost completely as an adsorbed layer formed. These results, the extensive work of others,<sup>51</sup> the good agreement of the surface-phonon dispersion relationships measured here with theory, and the reproducible He bound-state energies (selective adsorption), all indicate that the alkali-halide crystals are free of adsorbed layers of water at 300 K if treated as described. The single-crystal domains have been estimated to have dimensions of at least  $500 \text{ \AA}$ .<sup>34</sup>

### C. Scan curves and kinematical resolution

For interpreting the results and discussing the resolution it is convenient to project the kinematical restraints imposed by the equations for the conservation of momentum and energy onto a plot of  $\omega$  versus the total parallel momentum transfer  $\Delta\vec{K} = \vec{G} + \vec{Q}$ . For the present conditions of single-phonon in-plane inelastic scattering with a fixed angle  $\theta_{SD} = \theta_i + \theta_f = 90^\circ$  and with the phonon momentum also in the scattering plane, Eqs. (1a) and (1b) can be readily reduced to

$$\frac{\hbar\omega}{E_i} = \frac{\left[ \sin\theta_i \pm \frac{|\Delta\vec{K}|}{k_i} \right]^2}{\cos^2\theta_i} - 1, \quad (2)$$

where

$$E_i = \frac{\hbar^2}{2m} k_i^2$$

and the  $+$  and  $-$  signs refer to the direction of  $\Delta\vec{K}$  with respect to  $\vec{k}_i$ . Thus for a given  $k_i$  and  $\theta_i$ , Eq. (2) provides a relationship versus  $\Delta\vec{K}$  representing all the values  $\omega, \Delta\vec{K}$  allowed by conservation of ener-

gy and momentum. Figure 4 shows a series of such scan curves for different values of  $\theta_i$  ranging from  $0^\circ$  to  $90^\circ$  in steps of  $2^\circ$  for scattering of He with  $k_i = 6.00 \text{ \AA}^{-1}$ . On the same extended-zone plot are shown Rayleigh dispersion curves taken from a least-squares fit to the present experimental measurements for scattering from LiF along the  $\langle 100 \rangle$  direction. If single-phonon interactions with such phonons occur, then all points at which a given scan curve intersects the Rayleigh curves will lead to intensity maxima in the time-of-flight spectrum at times corresponding to the values of  $\hbar\omega$ . Figure 4 also shows the angles at which the specular peak, corresponding to  $\omega = 0$  and  $\Delta\vec{K} = 0$ , as well as the diffraction peaks, corresponding to  $\omega = 0$  and  $\Delta\vec{K} = \pm\vec{G}_{11}$ , occur. Note also that conservation of energy restricts creation events to frequency  $|\omega|$  less than  $2.86 \times 10^{13}$  rad/sec (corresponding to the incident beam energy of 18.8 meV).

Figure 4 indicates that for small  $\theta_i$  (near normal incidence) the scan curve extends over several Brillouin zones. This large amount of momentum information is obtained at the expense of frequency resolution, especially for creation events with large energy transfer. On the other hand for large  $\theta_i$  (corresponding to grazing incidence) only a narrow range of  $\Delta\vec{K}$  is probed but with improved resolution of  $\omega$ . In the extreme case of  $\theta_i = 90^\circ$  a constant- $\Delta\vec{K}$  scan at  $-k_i$  would be achieved.

Examination of Fig. 4 reveals another kinematic factor influencing the investigation of surface pho-

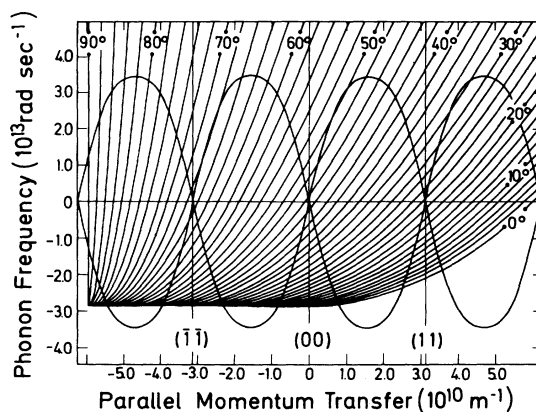


FIG. 4. Scan curves for scattering of He from LiF(001) along the  $\langle 100 \rangle$  azimuth. The parabolic scan curves ( $k_i = 6 \text{ \AA}^{-1}$ ,  $\theta_i = 0^\circ$  to  $90^\circ$ ) are superimposed on Rayleigh-phonon dispersion curves taken from a least-squares fit to the present experimental data. Annihilation events are to be found in the upper half-plane ( $\omega > 0$ ) and creation events in the lower half-plane ( $\omega < 0$ ). To the right and left of each reciprocal-lattice rod are located the forward ( $Q > 0$ ) and backward ( $Q < 0$ ) events, respectively.

nons. At about  $\theta_i = 33^\circ$ ,  $50^\circ$ , and  $68^\circ$  the scan curves are tangent to the Rayleigh dispersion curves for annihilation events. If the intensity between the diffraction peaks is due only to inelastic scattering with Rayleigh phonons then there should be an enhancement in the intensity of the angular distributions because of the increased overlap of the two curves at these angles. Benedek has called this rainbowlike effect kinematic focusing.<sup>52</sup> At these same angles the energy-loss spectra will show a correspondingly broadened peak. By the same argument we expect an optimal resolution whenever the scan curves cross a dispersion curve at right angles.

With the aid of the scan curves we can also investigate the kinematic smearing resulting from the finite spread in the incident angles and velocities. The effect of angular spread will have the greatest effect near kinematic focusing angles and the least effect at right-angle crossings. Since the nominal incident angular spread was  $0.20^\circ$  (see Table II) and the actual spread even less, we can see from Fig. 4 that the effect of kinematic averaging on phonon frequencies and momenta from angular smearing is negligible ( $<1\%$ ) except possibly at the angles for kinematic focusing.

The kinematic smearing of phonon frequencies resulting from a finite-velocity spread is illustrated in Fig. 5. There we have shown scan curves for two different  $k_i$  values, 5.88 and 6.12, representing a spread of  $\pm 2\%$ . It is interesting to note that for each angle there is a value of  $\omega, \Delta\vec{K}$  for which this kinematic smearing almost disappears. Since the ac-

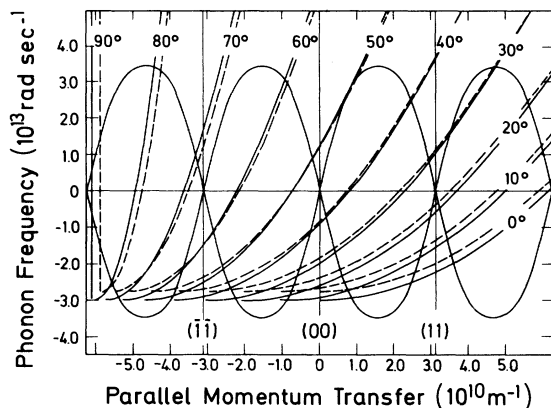


FIG. 5. Representation of the kinematic smearing to be expected due to a non-negligible velocity spread in the incident beam. Scan curves are drawn for  $k_i = 6.12 \text{ \AA}^{-1}$  (solid curves) and  $5.88 \text{ \AA}^{-1}$  (dashed curves) representing a 4% spread (FWHM). The actual velocity spread was considerably less (0.8% FWHM). Phonon dispersion curves are again a least-squares fit to the LiF(001) data along the  $\langle 100 \rangle$  directions.

tual velocity spread was only  $\pm 0.4\%$  the effect of the finite-velocity spread can be largely neglected.

#### D. Experimental time-of-flight and angular resolution

In addition to the kinematical resolution discussed above we must also consider the uncertainties arising from the nonideality of the time-of-flight apparatus in detecting energy transfer. Two effects have to be considered. For one we must make allowance for the fact that since the time-of-flight spectrum does not probe the energy transfer directly, the smearing of the energy loss  $\delta\hbar\omega$  for a given time-of-flight resolution  $\delta t$  will depend on  $\hbar\omega$ . As we shall see below  $\delta t$  is nearly constant over a relatively wide range of final velocities. From conservation of energy we calculate

$$\frac{\delta\hbar\omega}{E_i} = -2 \left[ 1 + \frac{\hbar\omega}{E_i} \right]^{3/2} \frac{\delta t}{t_{el}}, \quad (3)$$

where  $t_{el}$  is the time of flight for elastic scattering. For elastic scattering  $\delta\hbar\omega/E_i$  is given simply by  $2\delta t/t_{el}$ . For inelastic scattering  $\delta\hbar\omega/E_i$  goes from zero for extreme creation events to about  $6\delta t/t_{el}$  for an annihilation event with  $\hbar\omega = E_i$ .

The time-of-flight resolution  $\delta t$  is limited by a number of experimental factors. An estimate may be made of  $\delta t$  for a near-elastic event. First we consider the source velocity distribution which at 950 m/sec and  $\Delta v/v = 0.8\%$  contributes a time spread at the detector of 16  $\mu\text{sec}$ . Secondly there is the chopper-gate time of the 7.5-cm-radius chopper which had 0.25-mm slits and rotated at 150 Hz. For the nominal  $0.20^\circ$  FWHM incident beam (see Fig. 3 and Table II) the effective beam-spot diameter at the chopper was 0.53 mm (or 0.29 mm for the effective  $0.11^\circ$  FWHM) leading to a pulse of duration 7.5  $\mu\text{sec}$  (respectively, 4.1  $\mu\text{sec}$  FWHM). A third source of smearing stems from the finite length of the ionizer which was estimated to be 1 cm contributing an additional time uncertainty of about 11  $\mu\text{sec}$  at  $v = 950$  m/sec. The root mean square of these three widths yields an overall time uncertainty of 21  $\mu\text{sec}$  or  $\delta t/t \approx 1.2\%$  for elastic scattering and is in good agreement with the measured spread of the specular beam of 3–4 channels (21–28  $\mu\text{sec}$ ). For inelastic scattering  $\delta t/t$  will be smaller for creation events and larger for annihilation events because of the differences in  $t$ .<sup>47</sup> The detection resolution was ultimately limited by the multichannel scalar channel width of 6.9  $\mu\text{sec}$ .

In Fig. 6 we show a time-of-flight spectrum (scattered intensity as a function of flight time from chopper to detector) and compare it with the same

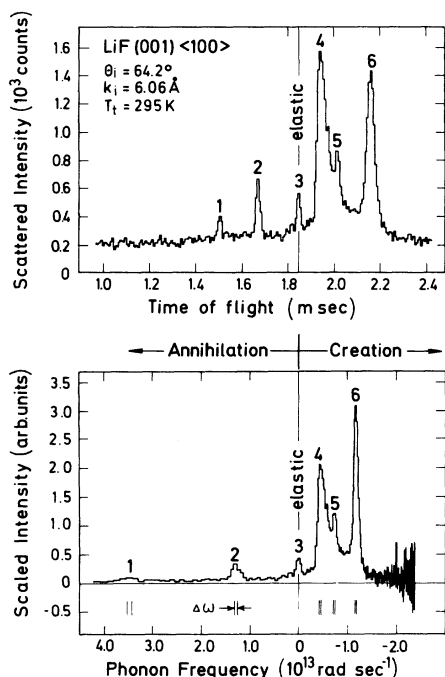


FIG. 6. Top: TOF trace taken under typical conditions. Maxima due to three creation events—peaks (4–6)—and two annihilation events—peaks (1 and 2)—appear to be present at this incident angle. In fact, peak 2 may be attributed to a “D spurion.” Bottom: Same data transformed to a plot of signal intensity as a function of phonon frequency. The concomitant scaling greatly affects relative peak heights. Frequency resolution varies with phonon frequency—estimated values are shown for the different peaks.

spectrum transformed onto the energy scale,

$$f_\omega(\omega) = f_t(t(\omega)) \frac{dt(\omega)}{d\omega}. \quad (4)$$

The Jacobian is simply given by

$$\left| \frac{dt}{d\omega} \right| = \hbar t_{td}^3 / m l_{td}^2,$$

where  $t_{td}$  is the inelastic time of flight (TOF) and  $l_{td}$  the distance from target to detector. This Jacobian factor leads to a relative enhancement in the TOF spectra of annihilation-event amplitudes as shown in Fig. 6. This figure also shows the estimated energy resolution for each of the peaks.

Note finally that this experimental uncertainty must be folded with the kinematic resolution discussed in the previous section, which compensates to some extent the energy smearing at large  $\omega$ . The actual data analysis was carried out by transforming each TOF spectrum into an energy spectrum and extracting  $\hbar\omega$ .  $Q$  was then calculated from the conservation equations.

The angular resolution of the apparatus was investigated as described in a previous publication.<sup>34</sup> The measured halfwidths for NaF along the <100> directions were found to be  $0.11^\circ$  for the specular peak and  $0.16^\circ$  and  $0.21^\circ$  for the (11) and  $(\bar{1}\bar{1})$  peaks, respectively. The specular peak is unaffected by the velocity spread and provides a base measure of the angular resolution if we neglect any small additional broadening due to the finite coherence length on the crystal. Since the detector is immobile the halfwidth of  $0.11^\circ$  is actually that measured by rotating the crystal and corresponds (for specular scattering) to one-half the angular spread which would have been measured with a movable detector. An accurate *a priori* estimate of the expected angular resolution is complicated by (1) the fact that the 13-mm entrance slit to the detector ionization cage was wider than the effective area seen by the mass spectrometer which had an entrance slit of only 3 mm, and (2) by the convolution of geometrical, viewing, and velocity-smearing factors.

For inelastic events, a simplified treatment<sup>47</sup> shows that the angular spread for annihilation events is always less than that of the associated diffraction peak, whereas for creation events it is always greater than and increasingly so with increasing phonon frequency.

#### E. Calibration procedures

Since the primary aim of the present study was to determine the surface-phonon spectrum it was not necessary to carry out an absolute calibration of the detector sensitivity. However, in the course of the LiF experiments it was estimated that the specular intensities were reproducible on a day-to-day basis to better than 30% and thus within these limits the relative TOF intensities can be compared. Because of Jacobian effects discussed above the area  $\int f(t)dt$  under the peaks and not the amplitudes should be compared. In the NaF and KCl experiments the detector sensitivity was calibrated daily by admitting He of known pressure into the detector chamber through a calibrated leak. The beam intensity was also monitored and the measured intensities were adjusted correspondingly. These will be referred to as renormalized TOF spectra.

Angular scans similar to those shown in Fig. 7 were taken periodically. From the angular spacing of the diffraction peaks the incident wave vector could be determined and compared with the direct TOF measurements. The beam velocity determined in this way agreed to better than 1% with a direct determination based on the TOF measured over a 6-m flight distance.

For all inelastic scattering measurements, the

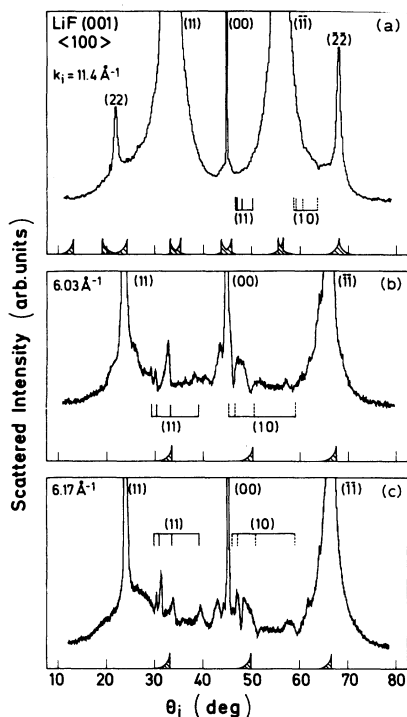


FIG. 7. Representative measurements of signal intensity as a function of incident angle ( $\theta_i + \theta_f = 90^\circ$ ) as different values of the incident-beam wave vector. Vertical bars mark selective-adsorption angles via  $G_{11}$  and  $G_{10}$  for the four bound states of He-LiF(001). Shaded wedges at the bottom of the traces show the expected angles and approximate shape of features due to kinematical focusing; these features are roughly  $10^3$  lower in intensity than the elastic peaks. For high enough incident energies (top trace) kinematical focusing involving both phonon creation and annihilation is possible.

TOF of the elastic scattering peak was registered before and after each run by rotating the crystal to an elastic scattering peak to check the incident-beam velocity.

### III. PRELIMINARY RESULTS

A number of exploratory experiments were performed to determine the most favorable conditions for observing single-phonon TOF spectra. Since these results may be of interest they are briefly described here.

#### A. Angular distributions

Figure 7 shows angular distributions taken at three different beam energies. The vertical scale has been greatly expanded to display the small inelastic features among the diffraction peaks. The angular

distribution at the top [Fig. 7(a)] was taken with the nozzle-beam-source temperature at 300 K ( $E_i \simeq 68$  meV) and with a stagnation pressure of 200 atm. Under these conditions the speed ratio is expected to be  $S=75$  corresponding to a velocity spread of 2.2%. The specular peak is less intense than the first-order diffraction peaks as was expected from the work of Boato, Cantini, and Mattera.<sup>53</sup> Velocity dispersion will broaden the first-order diffraction peaks by no more than  $0.25^\circ$  for the above velocity resolution. The broad bases of the diffraction peaks seen in Fig. 7(a) therefore may be attributed totally to inelastic scattering. The lack of detailed structure within these inelastic tails indicates that multiphonon scattering dominates at this incident-beam energy.

The bottom two curves are typical of the angular distributions which result if the beam source is cooled to near-liquid-nitrogen temperature. The broad bases of the diffraction peaks have diminished in amplitude and much new detailed structure has appeared among the diffraction peaks. This inelastic structure has been discussed elsewhere.<sup>34</sup> Some of the maxima and minima could be attributed to an enhancement or attenuation of the inelastic scattering by elastic selective adsorption which is predicted to occur at the angles indicated by the brackets. Thus in a classical description we attribute the maxima to particles which are trapped in a selectively bound state of the atom-surface potential and travel distances up to about 500 Å along the surface before they are brought out of resonance by an inelastic single-phonon process. We have designated this process selective desorption.<sup>34</sup> The same conservation conditions hold for these indirect inelastic events as for the direct events. In a quantum description we expect the direct and indirect channels to interfere and the increase in intensity implies constructive interference or possibly that the amplitude of the resonant process is dominant.<sup>54</sup> We observe that usually minima rather than maxima occur for selective adsorption with out-of-plane reciprocal-lattice vectors. Here the classical probability of reaching the detector is diminished, implying destructive interference. The selective adsorption-desorption model explains many but not all the structures in the spectra, especially the large shoulders near the specular peak. As indicated from a comparison of the two angular scans in Figs. 7(b) and 7(c), the relative amplitudes of the selective desorption structures are sensitively dependent on the beam energy. This is not surprising in view of the interference between the various contributions discussed above.

In addition to selective desorption we also have investigated the role of kinematic focusing.<sup>52,55</sup> An-

gles at which kinematic focusing can occur and the approximate expected angular distributions of these contributions are indicated by the shaded wedges at the bottom of Fig. 7. As discussed below there is no evidence that kinematic focusing has a significant effect on the polar-angular distributions for LiF. The effect of kinematic focusing on the NaF angular distributions has been discussed elsewhere.<sup>55</sup> The angular distributions also did not significantly depend on the target temperature.

### B. TOF spectra

TOF spectra taken with the He-beam source at  $T_0 = 300$  K giving an incident-beam wave vector of  $11.4 \text{ \AA}^{-1}$  ( $E_i = 67$  meV) showed no resolved structure. Broad peaks were found which were shifted to the annihilation or creation side depending on the

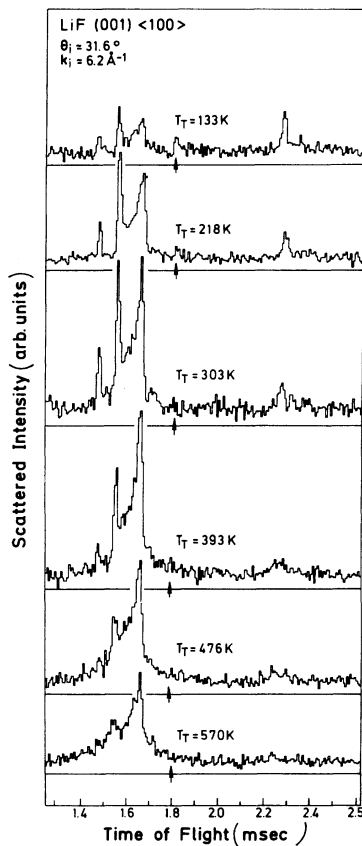


FIG. 8. Series of TOF spectra recorded for different values of target temperature. The single creation peak (right-hand side of spectra) is affected much differently than the three annihilation peaks. The small arrow marks the chopper-detector flight time of elastically scattered atoms. The constant background has been suppressed in these spectra.

scattering angle. From the distributions it was not possible to infer whether surface or bulk phonons or both were predominantly involved. As discussed below the predominance of multiphonon processes is expected on the basis of theoretical estimates.

Figure 8 shows a series of normalized spectra for six different target temperatures between 133 and 570 K. For comparison the bulk melting temperature of LiF is 1115 K and the surface and bulk Debye temperatures are about 500 and 720 K, respectively. In all the spectra three annihilation peaks and one creation peak are observed and show different trends with temperature. The creation peak to the far right is sharpest at the lowest temperature and becomes weaker and broader with increasing temperature. This weakening reflects the transition from a single-phonon interaction at low temperatures to multiphonon interactions at higher surface temperatures. Only the single-phonon interactions produce sharp TOF maxima.

If the resolution were perfect it should be possible to determine surface-phonon lifetimes  $\tau$  from the widths of single-phonon peaks such as the 133-K creation peak at 2.3 msec (Fig. 8). From this peak we can only make an order-of-magnitude lower-limit estimate of  $\tau \approx \hbar/\Delta E \approx 2 \times 10^{-11}$  sec, which is consistent with a crude estimate of  $10^{-12}$  sec from scaling surface-acoustic-wave attenuation factors.<sup>56</sup>

The three annihilation peaks in Fig. 8 appear to have a different temperature dependence, passing through a maximum near room temperature. The increase at low temperatures is in accord with the population changes for a Bose distribution. At high temperature the overall decrease in inelastic intensity and smearing of the peak structure is again attributed to multiphonon processes.

The overall trends observed here agree with the predictions of Meyer,<sup>57</sup> who showed that even at high surface temperature, where multiphonon processes are probable, single-phonon peaks can be expected. Weare<sup>58</sup> predicted that single phonons will dominate for

$$\frac{m}{M} \frac{E_{iz}}{k_B \Theta_D} \frac{T}{\Theta_D} < 0.01, \quad (5)$$

where  $m$  is the mass of the beam projectile,  $M$  is the mass of a surface atom,  $k_B$  is the Boltzmann constant, and  $E_{iz}$  the normal component of the energy. With a surface Debye temperature of  $\Theta_D \approx 500$  K (see Table I) this estimate yields a value of roughly 100 K for  $T$ , in reasonable agreement with the observations. Since the annihilation-peak intensities were optimum at  $T = 300$  K, all the TOF studies were carried out at this temperature.

The Rayleigh dispersion relation is actually a



## IV. MEASUREMENTS OF DISPERSION CURVES

A. Along the  $\langle 100 \rangle$  and  $\langle 110 \rangle$  symmetry directions in LiF

In the present study we have emphasized the  $\langle 100 \rangle$  direction of LiF. A total of 94 spectra were measured at incident angles between  $18.0^\circ$  and  $72.2^\circ$  and for wave vectors which varied between  $5.97 \text{ \AA}^{-1}$  and  $6.25 \text{ \AA}^{-1}$ . Figure 11 shows a series of TOF spectra taken at incident angles near the (11) diffraction peak (see Fig. 4). The spectra taken at angles two degrees removed from the diffraction peak at  $\theta_i = 22.0^\circ$  and  $26.0^\circ$  reveal, at flight times corresponding to elastic scattering, a small peak with a count rate of only about 300 Hz (compared with a diffraction-peak intensity of about  $10^4$  Hz). This small elastic scattering intensity is attributed to elastic scattering from crystal imperfections; slightly tilted crystal facets and scattering from steps and randomly distributed imperfections can account for this intensity. Examination of Fig. 11 indicates that

with a further increase of  $1^\circ$  in  $\theta_i$  away from the diffraction peak, this elastic scattering contribution disappears into the background noise.

The spectra in Fig. 11 also contain spurious peaks of another sort which will be discussed at the end of this section. These peaks, which are called "D spurions," are indicated by a *D* in Fig. 11. The other maxima in Fig. 11 can be assigned to an interaction with surface phonons with a dispersion close to that of theoretical estimates. The assignment of  $\hbar\omega$  and  $Q$  values to each of the peaks can be carried out with the aid of the scan curve shown in Fig. 4. The following trend thus emerges as the angle is swept through the diffraction peak. At  $18^\circ$  creation events corresponding to forward and backward momenta dominate. With increasing angle moving towards the diffraction angle these maxima merge together, shift to smaller energy transfer, and increase in intensity. Analogous behavior appears on the other side of the diffraction peak where the inelastic scattering peaks correspond to annihilation events.

Figure 12 shows a series of spectra taken at five

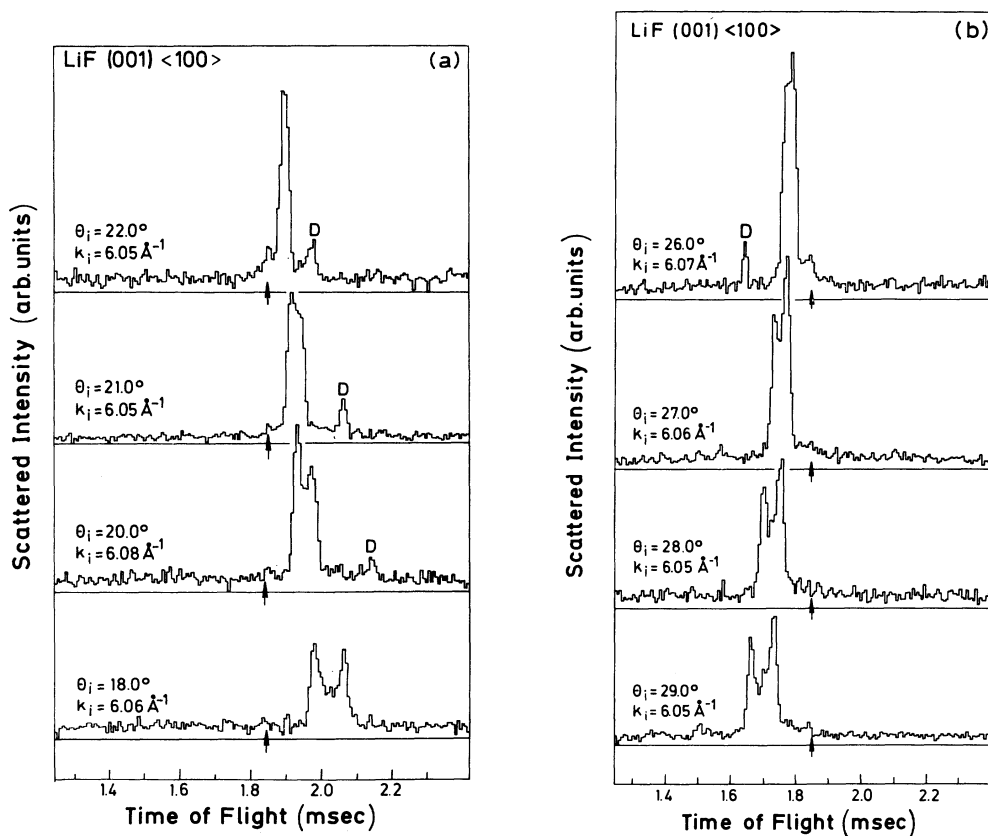


FIG. 11. TOF traces for scattering at incident angles near the  $G_{11}$  diffraction angle ( $\theta_i \approx 23.6^\circ$ ). As expected from the scan curves, Fig. 4, the inelastic scattering is dominated by creation events at incident angles less than that of  $G_{11}$  diffraction (trace *a*) and annihilation at larger angles (trace *b*). The small constant background of these spectra has been suppressed. The small arrow marks the chopper-detector flight time of elastically scattered atoms. *D* spurions (see text) have been labeled with a *D*.

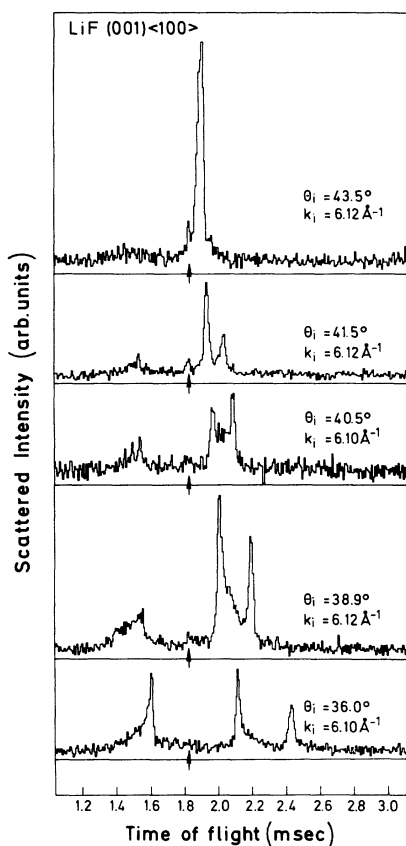


FIG. 12. Similar TOF traces as those of Fig. 11, but for a range of incident angles near the specular reflection.

angles near a sharp resonant bound-state maximum for the  $\nu=0$  lowest-bound He surface state at about  $39^\circ$ . At  $\theta_i=36^\circ$  the spectrum shows a nearly symmetric structure with respect to the expected location of the elastic peak, characterized by a sharp rise in intensity and a slowly decreasing tail. This broad tail lies in the region of small  $Q$  where bulk modes are expected. These tails and the plateau between the two largest Rayleigh peaks in the spectrum at  $38.9^\circ$  are considered as direct evidence that bulk phonons at the surface are also contributing to the interaction. The dropoff shown by the tails is expected from the Bose population factor. At  $38.9^\circ$  we observe that the inelastic scattering intensity especially on the creation side is enhanced by selective desorption which, at the measured wave vector, is calculated to occur at  $\theta_i=39.1^\circ$ . The spectrum at  $\theta_i=43.5^\circ$  shows the rise in inelastic scattering intensity also observed in Fig. 11 as the scan curve approaches one of the specular or diffraction peaks. Finally we note that no spurious (incoherent elastic or  $D$ ) peaks are present in these spectra, which are far removed in angle from the diffraction peaks.

Figure 13 shows a series of spectra taken at larger (more grazing) incident angles lying on both sides of the  $(\bar{1}\bar{1})$  diffraction peak. The scan curves for the series of spectra, shown in Fig. 14, cross the dispersion curves at smaller angles of intersection than in the vicinity of the  $(\bar{1}\bar{1})$  peak and at smaller values of  $\hbar\omega$ . Thus the conditions are particularly favorable for observing kinematical focusing which is expected at about  $67.5^\circ$ . Starting from the small-angle end we observe at  $63.2^\circ$  and  $64.2^\circ$  altogether three maxima all on the creation side. Of these the central peak lies at values of momentum transfer between the Rayleigh peaks and can probably be attributed to a feature in the bulk-phonon spectrum. This central peak corresponds to bulk phonons with projection of momentum parallel to the surface of  $Q \approx 0$ . It may be due to a multiphonon interaction.

The spectrum at  $67.3^\circ$  is taken on the large- $\theta_i$  side of the  $(\bar{1}\bar{1})$  peak. Here annihilation events dominate the spectrum. The spectra at  $67.3^\circ$  and  $65.2^\circ$  show an approximate inversion symmetry with respect to the elastic peak, the only major deviation being the appearance of an additional peak on the annihilation side as expected from the scan curves. At  $67.5^\circ$  we expect kinematic focusing to lead to a broad diffuse structure halfway between the two outer annihilation peaks of the  $67.3^\circ$  spectrum. The transition through the kinematical focusing near  $67.5^\circ$  may be gauged from the spectra at  $67.3^\circ$  and  $68.3^\circ$ . As discussed in the preceding section, it is the two highest-frequency annihilation peaks which coalesce and disappear. The overall intensity loss, while by no means negligible, is nonetheless not so pronounced with respect to the other annihilation peak as in the case of azimuthal-angle kinematical focusing. In the polar-angle distribution the effects of kinematical focusing are thus outweighed by bound-state resonant features.

All of the maxima (with the exception of those due to elastic scattering from crystal imperfections) have been evaluated for their effective  $\hbar\omega$  and  $Q$  values. The result of all determinations is shown in an extended-zone diagram in Fig. 15. There it is seen that to first approximation all points seem to fall on either a Rayleigh dispersion curve or on anomalous dispersion curves. These additional anomalous dispersion curves are only observed near the diffraction peaks and are characterized by both  $Q$  and  $\hbar\omega$  having the same sign. A similar anomalous dispersion curve was also observed for NaF and had the same shape and character as shown in Fig. 15 (see Fig. 23). Since theory predicts neither bulk phonons nor surface phonons in the region of this anomalous curve, another explanation must be sought.

The fact that these events occur only near the dif-

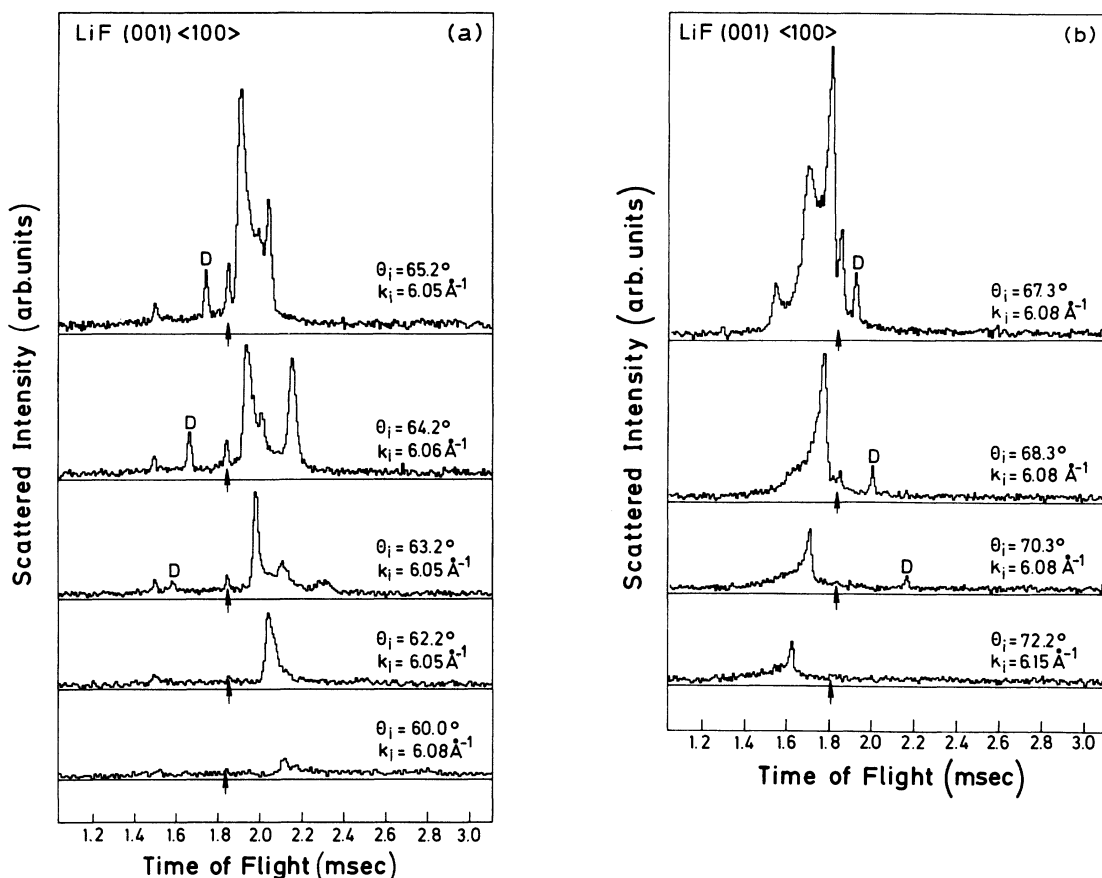


FIG. 13. TOF spectra similar to those of Fig. 11 but now for incident angles near the  $G_{\bar{1}\bar{1}}$  diffraction angle. In this range of angles, a small maxima appears at the elastic flight time (arrow), probably arising through incoherent elastic scattering from surface irregularities or from the crystal edges. Note the broadening of the two highest-frequency (left-most) maxima in the  $67.3^\circ$  spectrum. This is seen in Fig. 14 to result from the nearly tangent scan curves and dispersion curves near the kinematical-focusing angle.

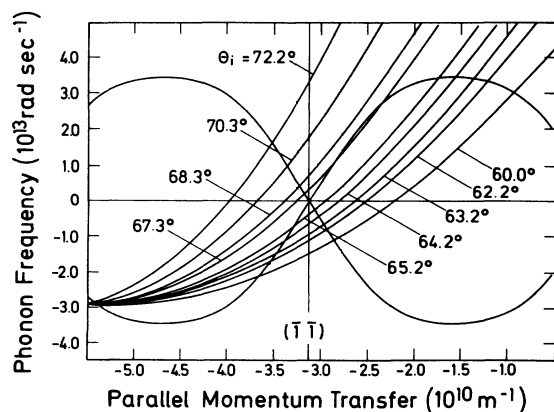


FIG. 14. Scan curves for the TOF spectra of Fig. 13.

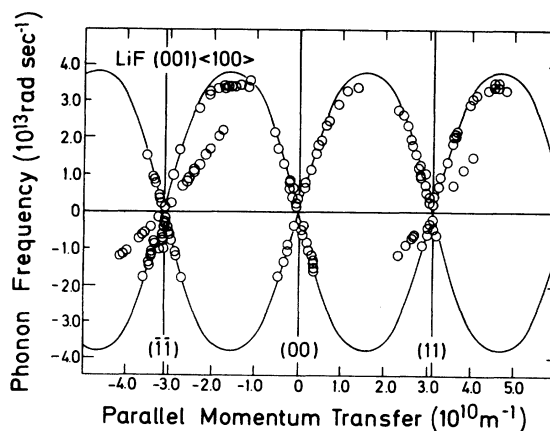


FIG. 15. Compilation in an extended-zone plot of frequency and parallel momentum for each of the sharp maxima observed in the LiF TOF spectra. Theoretical predictions by Chen, de Wette, and Alldredge (Ref. 7) for LiF Rayleigh-phonon dispersion curves are shown (solid-line curves). With the exception of the  $D$  spurions (see text), the data conform well to the Rayleigh curves.

fraction peaks suggests that they may be due to some sort of diffraction phenomenon involving the incident helium beam.<sup>47,59</sup> The presence of such effects is, in fact, not surprising if the beam has a non-negligible velocity distribution. The apparatus then functions as a monochromator: Diffraction from the surface disperses the beam in angle according to its velocity distribution and the narrow beam collimation selects a particular velocity. The resulting peak in a TOF spectrum is thus due entirely to elastic scattering but may, depending on the velocity distribution, be considerably shifted from the median elastic scattering flight time. Incorrectly assuming the incident beam to be monoenergetic then leads to the conclusion that some unexpected inelastic scattering is taking place. Such effects have been previously seen in inelastic neutron scattering where the nonexistent anomalous quanta are dubbed "spurions." In view of their deceptive nature we are led to call them "*D* spurions."

We can easily estimate the effect of *D* spurions on our spectra. Consider a contribution from incident He atoms with a wave vector  $\hat{k}_i \neq k_i$  where  $k_i$  is the most probable velocity. If we incorrectly assume that such particles are due to  $k_i$  then we would assign to these diffracted particles a TOF shift given by

$$\Delta t = \frac{ml_{cd}}{\hbar} \left[ \frac{1}{k_i} - \frac{1}{\hat{k}_i} \right], \quad (6)$$

where  $l_{cd}$  is the distance from chopper to detector. The apparent final wave vector is then calculated to be

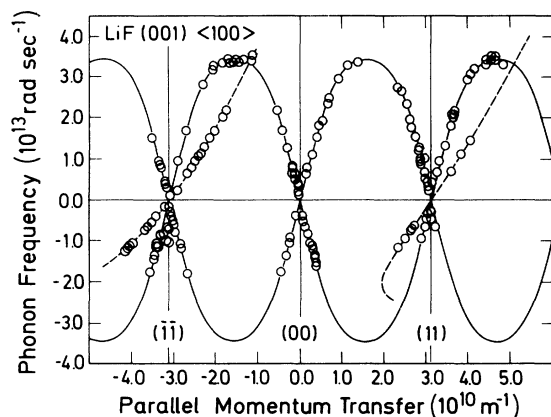


FIG. 16. Extended-zone compilation similar to that of Fig. 15. "Dispersion relations" for *D* spurions [Eqs. (8) and (9)] have been plotted as dashed-line curves. Solid-line curves are a least-squares fit to the experimental data, which gives a zone-boundary ( $\bar{M}$ ) frequency of  $3.45 \times 10^{13}$  rad/sec.

$$\frac{k_f}{\hat{k}_i} = \left[ \frac{l_{cd}}{l_{td}} \left( \frac{\hat{k}_i}{k_i} - 1 \right) + 1 \right]^{-1}, \quad (7)$$

which correctly yields  $k_f = k_i$  when  $\hat{k}_i = k_i$ . With the usual manipulations we then would assign this event to the following "frequency" and "wave vector":

$$\frac{2m\omega}{\hbar \hat{k}_i^2} = \left[ \frac{k_f}{\hat{k}_i} \right]^2 - 1, \quad (8)$$

$$\frac{|\Delta \vec{K}|}{\hat{k}_i} = \frac{K_f}{k_i} \cos \theta_i - \sin \theta_i. \quad (9)$$

The scattering angle  $\theta_i$  is calculated from the diffraction relation. These two equations provide a parametrized relation  $\omega(|\Delta \vec{K}|)$  which may be superimposed on an extended-zone plot in much the same manner as the phonon dispersion curves. Figure 16 shows that these *D*-spurion "dispersion curves" agree well with the measured points. A similar good agreement was also found in the case of NaF. Note that the amplitude of the *D*-spurions reflects the amplitude of the contributing portion of the incident-beam-velocity distribution. That *D*-spurion amplitudes are roughly as large as the true phonon-induced peaks shows that the tails of the velocity distribution are roughly 3 orders of magnitude lower than the peak value. For this reason and from intensity estimates we feel that the *D* spurions are likely due to a beam formed by the residual gas in the first pumping stage.

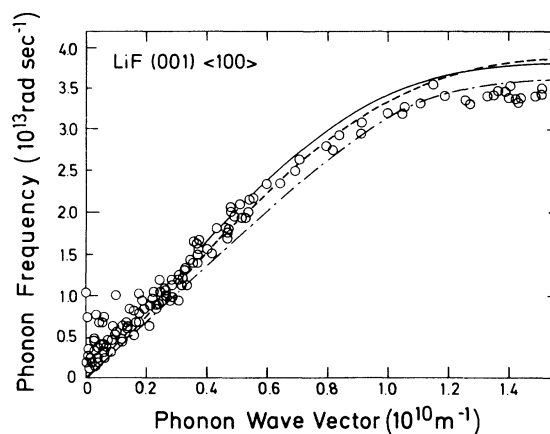


FIG. 17. Plot in the irreducible portion of the Brillouin zone of the experimental data of Fig. 16. Theoretical Rayleigh dispersion curves from Benedek (Ref. 8) (dashed-line curve) and Chen, de Wette, and Alldredge (Ref. 7) (solid-line curve) are shown. Dotted-dashed curve gives the most recent results from Benedek, Miglio, and co-workers (Refs. 33, 60, and 61). *D* spurions have been suppressed.

A close examination of the other experimental points reveals two marked deviations from the Rayleigh curves. The one significant deviation has to do with the occurrence of low- $Q$  bulk-band features which are most frequently observed as creation processes near the  $(\bar{1}\bar{1})$  diffraction peak. A similar propensity for bulk-mode creation near diffraction peaks was observed in NaF.

The other deviation at large- $Q$  values is more clearly seen in the reduced-zone plot shown in Fig. 17. For comparison we have also shown dispersion curves predicted by the theoretical calculations of Chen, de Wette, and Alldredge<sup>7</sup> and of Benedek and co-workers.<sup>33,60,61</sup> The agreement with the theoretical curves is good from  $Q=0$  out to about  $Q=0.8 \text{ \AA}^{-1}$ . The largest discrepancy to both theories is at the zone boundary where the experiments level off to a constant value of  $3.4 \times 10^{13} \text{ rad/sec}$  compared to the theoretical predictions of about  $3.8 \times 10^{13}$

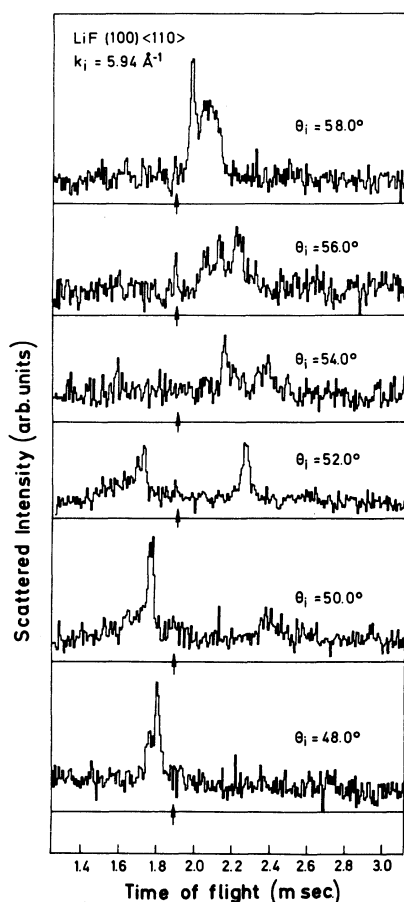


FIG. 18. TOF spectra for scattering from LiF(001) but now scattering in the  $\langle 110 \rangle$  azimuthal direction. Features are noticeably less distinct than in the  $\langle 100 \rangle$  azimuth (Figs. 11–13). Constant background has been suppressed. Small arrow marks the flight time for elastically scattered atoms.

rad/sec. The discrepancy is considerably larger than the frequency resolution of the apparatus and the random scatter of the points. This deviation is perhaps not so surprising since at the zone boundary the phonon wavelength is comparable to the lattice spacing and therefore the depth of penetration is of the order of only one atomic layer. Thus these phonons reflect critically the true microscopic atomic interactions at the surface. The several explanations which have been suggested to account for this discrepancy will be discussed in the last section.

The  $\langle 110 \rangle$  direction in LiF is of interest since lattice dynamics predict that the surface wave of lowest frequency is a shear horizontal mode and not a sagittally polarized mode as along the  $\langle 100 \rangle$  direction and along both directions in the other crystals studied. According to the calculations of Chen, de Wette, and Alldredge<sup>7</sup> the frequency of the sagittal-plane modes lies above the edge of the shear horizontal (SH) bulk band over most of the range of  $Q$ . Thus it was questionable if there would be any coupling to surface phonons in this case. Figure 18 shows a series of TOF spectra in the region of the specular and  $(\bar{1}\bar{0})$  maxima. We note that in all spectra sharp structures are observed which are generally quite similar to those found for the  $\langle 100 \rangle$  direction. However, the peak intensities are much lower, averaging only about 20–60% of the background intensity. One exception is  $\theta_i = 40.5^\circ$  at which angle a particularly strong selective desorption peak corresponding to the  $n=2$  state has been identified.<sup>76</sup> An extended-zone diagram giving all the measured points is shown in Fig. 19. Because of the low in-

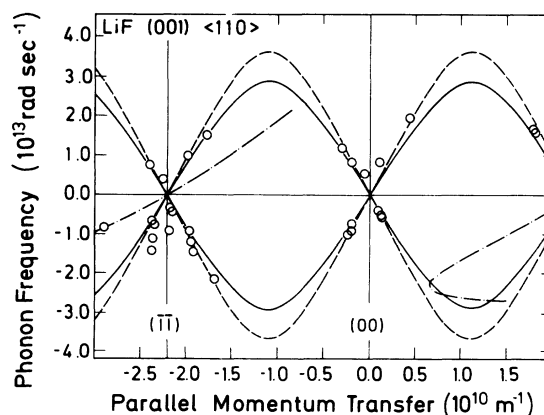


FIG. 19. Compilation in an extended-zone plot of the TOF maxima for LiF(001) in the  $\langle 110 \rangle$  direction. Unfavorable signal-to-noise ratio in this azimuthal direction precluded measurements near the zone boundary. Theoretical predictions from Chen, de Wette, and Alldredge (Ref. 7) for the sagittal plane  $S_7$  mode (dashed-line curve) and the shear horizontal  $S_1$  mode (solid-line curve) as well as the  $D$ -spurion curves (dotted-dashed curve) are shown. The leftmost point is a  $D$  spurion.

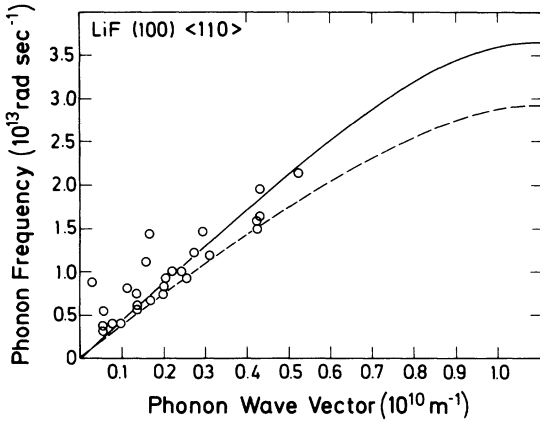


FIG. 20. Reduced-zone plot of the LiF(001)  $\langle 110 \rangle$  data. Theoretical predictions from Chen, de Wette, and Alldredge (Ref. 7) for the sagittal plane  $S_7$  mode (solid-line curve) and the shear horizontal  $S_1$  mode (dashed-line curve) are shown.

tensities, only low-frequency phonons could be resolved. Figure 20 shows a comparison between theory and experiment in a reduced-zone diagram. The theoretically predicted curves of Chen, de Wette, and Alldredge<sup>7</sup> for the  $S_1$  and  $S_7$  surface modes are shown for comparison. Unfortunately the larger scatter in the data points and the limitation of the data to low- $Q$  values makes it impossible to say whether it is one or the other or both of these modes which dominates the inelastic scattering.

#### B. Along the $\langle 100 \rangle$ symmetry directions in NaF

NaF is quite similar to LiF in most respects but the Debye temperature is  $\frac{2}{3}$  that of LiF. The maximum Rayleigh-mode frequency at  $\bar{M}$  is reduced by about the same ratio. However, at  $\bar{X}$  the Rayleigh frequency is even larger than at  $\bar{M}$ . Unlike LiF, the NaF(001) surface propagates true (sagittally polarized) Rayleigh modes in all azimuthal directions.

The TOF spectra measured with NaF were similar to those found for LiF although somewhat lower in intensity. Figure 21 shows a set of spectra taken

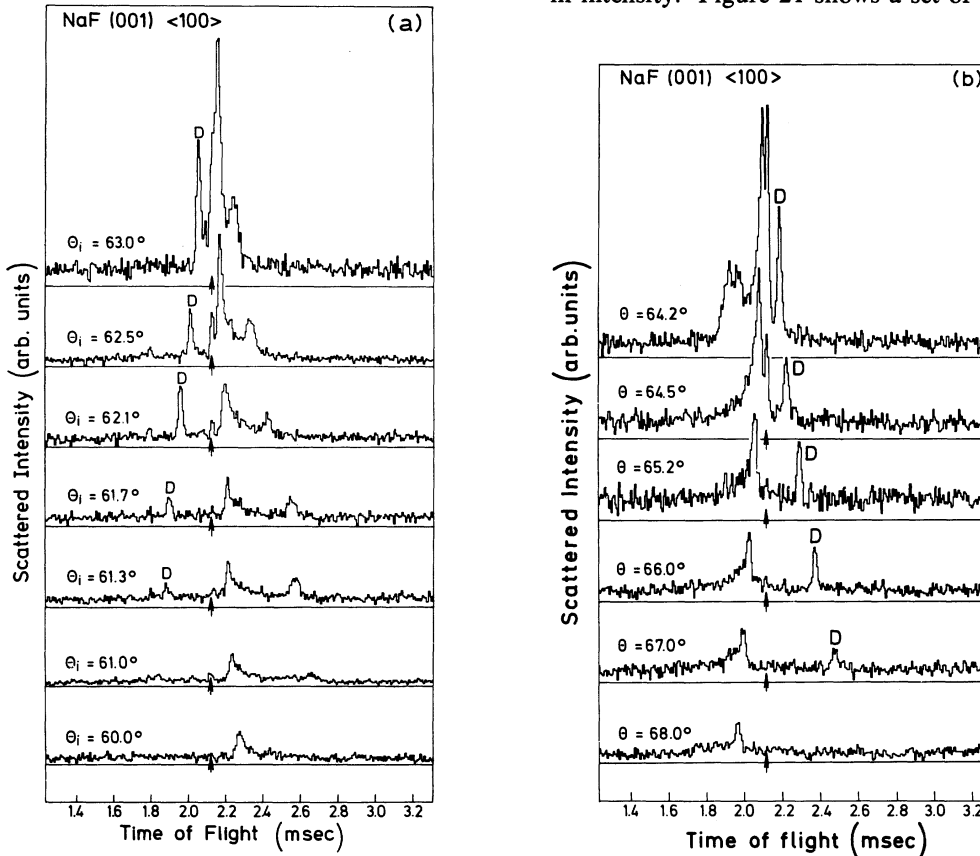


FIG. 21. TOF spectra for NaF(001) along the  $\langle 100 \rangle$  azimuth, taken at values of incident angle near the  $G_{11}$  diffraction angle ( $\theta_i \approx 63.7^\circ$ ). The spectra are similar to those for scattering from LiF(001) in this azimuth.  $D$  spurions have been marked with a  $D$ . The small arrow marks the flight time for elastically scattered atoms. Again, the constant background has been suppressed.

at large incident angles near the  $(\bar{1}, \bar{1})$  peak, located at  $\theta_i = 63.7^\circ$ . The corresponding scan curves are shown in Fig. 22. Some interesting features similar to those found for LiF are the bulk-phonon tails in the spectra  $\theta_i = 61.3^\circ, 61.7^\circ,$  and  $62.1^\circ$ . At  $62.5^\circ$  a distinct bulk-phonon peak is observable. The spectra at  $64.2^\circ$  and  $64.5^\circ$  illustrate how sensitively the spectra depend on the incident angle at angles where kinematic focusing is expected. At this angle the angular distributions do not show a clear resolution of kinematic focusing due to the dropoff in intensity in the vicinity of the diffraction peak. Kinematic focusing has been found at other angles in NaF and the evidence for this effect is discussed in another study.<sup>55</sup> The NaF data are summarized in an extended-zone plot in Fig. 23. The data again reveal a *D*-spurion dispersion relationship as with LiF.

Figure 24 shows a comparison of all the measurements with the theoretical calculations of Chen, de Wette, and Alldredge<sup>7</sup> and Benedek, Miglio, and co-workers<sup>33,60,61</sup> in a reduced-zone plot. For NaF there is good agreement with theory over the entire region and also at the zone boundary.

### C. Along the $\langle 100 \rangle$ directions in KCl

KCl is considerably softer than LiF as is evident from the much lower Rayleigh  $\bar{M}$  frequency of  $1.0 \times 10^{13}$  rad/sec ( $3.4 \times 10^{13}$  rad/sec for LiF). Because of the reduced frequency it therefore presents

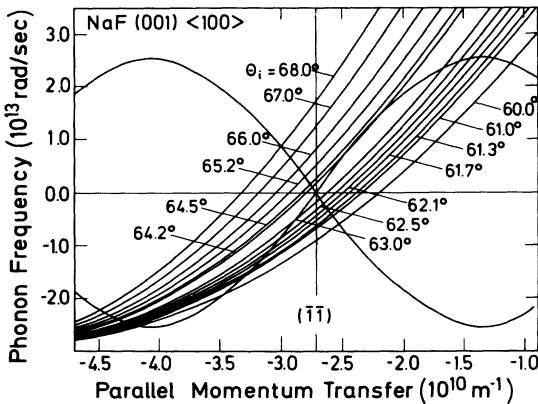


FIG. 22. Scan curves for the spectra of Fig. 21. Dispersion curves are a least-squares fit to the experimental data. Kinematical focusing is seen to occur at  $\theta_i = 64.2^\circ$ . Corresponding TOF spectra [Fig. 21(b)] show the highest-frequency annihilation peak to be quite broad, as expected, and to vanish at larger incident angles. The effect on the total scattered intensity (integration under the TOF spectrum) is, however, barely discernible because of the strong decrease in overall intensity in the vicinity of the diffraction peak.

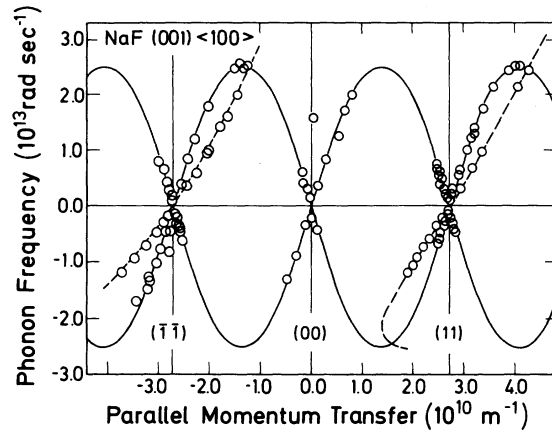


FIG. 23. Compilation in an extended-zone plot of TOF maxima in scattering from NaF. Solid-line curves are theoretical predictions by Chen, de Wette, and Alldredge (Ref. 7) for Rayleigh dispersion curves. In contrast to the results for LiF, agreement between experiment and theory is good throughout the Brillouin zone. Dispersion curves for *D* spurions are shown as dashed-line curves.

an extreme test of the resolution of the apparatus. An additional complication is purely kinematical; for KCl(001), the scan curves along the  $\langle 100 \rangle$  directions with  $k_i = 6 \text{ \AA}^{-1}$  are practically tangent to the forward annihilation and backward creation dispersion curves making measurements along these branches rather difficult. To alleviate this problem the beam angular halfwidth was reduced by a factor of 2 over the value used in the LiF measurements.

The angular distribution showed four diffraction

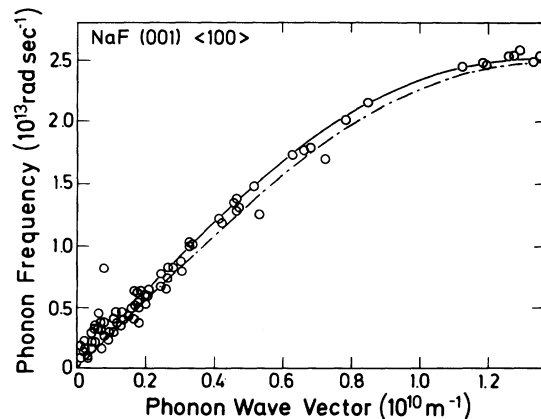


FIG. 24. Data of Fig. 23 replotted in the irreducible portion of the first Brillouin zone. Solid-line curve gives the dispersion for Rayleigh phonons as calculated by Chen, de Wette, and Alldredge (Ref. 7). More recent calculations by Benedek, Miglio and co-workers (Refs. 33, 60, and 61) are shown as a dotted-dashed curve.

peaks at  $17^\circ$  (22),  $32^\circ$  (11),  $58^\circ$  ( $\bar{1}\bar{1}$ ), and at  $73^\circ$  ( $\bar{2}\bar{2}$ ). The intensities were much lower than for LiF possibly due to the greater Debye-Waller factor. Structure and an overall increase in the inelastic background were only seen in the TOF spectra between  $40^\circ$  and  $50^\circ$  centered above the specular peak. For this reason most of the TOF spectra were taken in this region. Figure 25 shows some of the TOF spectra. The signal-to-background ratio was much lower than for LiF along the  $\langle 100 \rangle$  directions and for NaF along the  $\langle 100 \rangle$  directions and is roughly comparable to that found for LiF along the  $\langle 110 \rangle$  directions. The reduced inelastic scattering probability may be due to the inability of the He atom to exchange energy with the much heavier K and Cl atoms. Large clearly resolved TOF peaks are seen only at angles close to the specular peak.

Figure 26 shows an extended-zone plot of all the data available for KCl. Most of the points follow closely the Rayleigh curve out to the zone boundary. The exceptions are a number of points at higher fre-

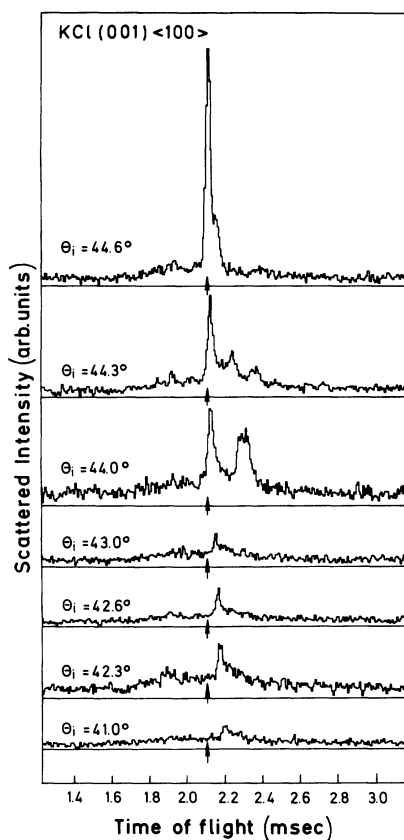


FIG. 25. TOF spectra for scattering from KCl. No  $D$  spurions were seen for this system. The elastic scattering flight time is marked with a small arrow. The constant background has again been suppressed.

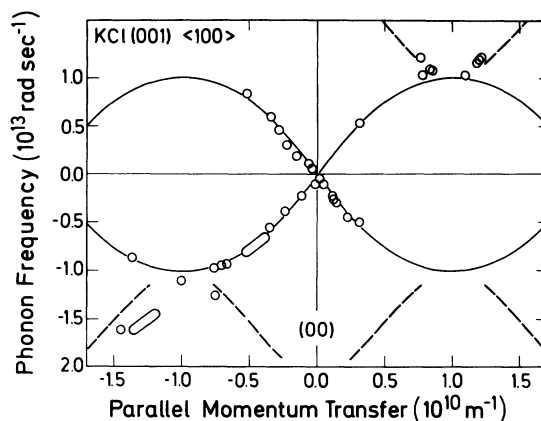


FIG. 26. Extended-zone plot of the TOF maxima for scattering from KCl. Exceptionally broad peaks are shown as elongated circles. Solid-line curves represent Rayleigh-phonon dispersion curves as calculated by Benedek and Galimberti (Ref. 45). Their "crossing mode" is shown as a dashed-line curve.

quency which lie in the bulk region. When plotted in the reduced-zone scheme of Fig. 27 it is seen that these high-frequency modes might be associated with the "crossing mode" theoretically predicted by Benedek and Galimberti.<sup>45</sup> This feature arises through the near match in the K and Cl masses. Were the match exact, the reciprocal lattice would be doubled in size; the "almost" match folds what would be the upper half of the Rayleigh mode back

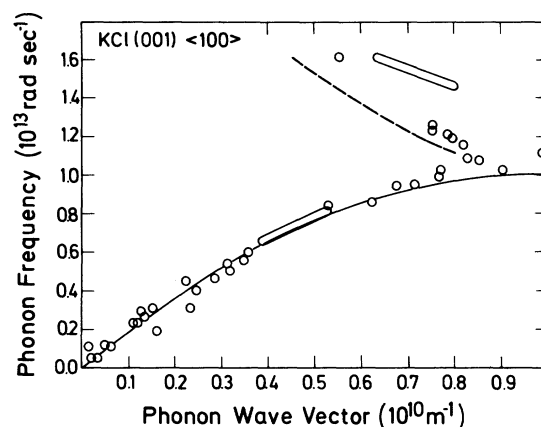


FIG. 27. Data of Fig. 26 replotted in the irreducible portion of the first Brillouin zone. Solid- and dashed-line curves are again the theoretical predictions for Rayleigh and crossing modes as calculated by Benedek and Galimberti (Ref. 45). High-frequency data points indicate scattering involving phonons of higher frequency than Rayleigh phonons.

onto the true first Brillouin zone, where it shows up as an enhancement of the transverse-acoustical bulk modes. No  $D$  spurions were detected for KCl, probably due to the lower diffraction intensities.

#### D. Experimental dispersion curves

For measurements in the  $\langle 100 \rangle$  azimuth of LiF, NaF, and KCl, the experimental measurements delineated the Rayleigh dispersion curves sufficiently well that a parametrized curve could be fitted to the data. An expression of the form

$$\omega = B_1 \sin \left[ \frac{\pi Q}{G_{11}} \right] + B_3 \sin \left[ \frac{3\pi Q}{G_{11}} \right] + B_5 \sin \left[ \frac{5\pi Q}{G_{11}} \right] \quad (10)$$

was employed. The values of  $B_1$ ,  $B_3$ , and  $B_5$  were determined from a least-squares fit to the experimental data with non-Rayleigh data points (deceptons and bulk modes) removed. No attempt has been made to match the slope at the  $\bar{\Gamma}$  point to the correct Rayleigh value. The results are shown in Table III. Error bars for random error, expressed in terms of frequency, are about 5% of the  $\bar{M}$  frequency as may be seen from Figs. 17, 24, and 27. A systematic error corresponding to one channel in flight time would shift the  $\bar{M}$  frequency by 0.12, 0.08, and  $0.05 \times 10^{13}$  rad/sec for LiF, NaF, and KCl, respectively.

#### V. DISCUSSION

The data presented in the preceding section represent the first complete measurement of surface-phonon dispersion curves. The alkali halides present an ideal meeting ground for experiment and theory. Clean ordered surfaces are easily prepared through cleaving and one is able to draw upon extensive experience with their elastic scattering behavior. For theoretical calculations they have the advantage that the interatomic forces are dominated by classical electrostatic interactions and thus are relatively easily modeled. The theoretical efforts can also utilize experience with fitting bulk-phonon dispersion data. Thus although the two theoretical

approaches<sup>6,9</sup> model the interatomic potentials in different ways, they have been able to produce essentially identical surface-phonon dispersion curves. The present experiments indicate that both of these theoretical models lead to correct Rayleigh-wave dispersion curves for NaF and KCl along the  $\langle 100 \rangle$  directions but overestimate the maximum frequency by about 10% in the case of LiF along the  $\langle 100 \rangle$  directions.

One possible explanation for the discrepancy is that it is due to surface relaxation,<sup>62</sup> which refers to the change in the lattice-layer spacing near the surface. According to the extensive calculations of Benson and Claxton<sup>63</sup> the positive ions at the surface of the alkali halides are drawn inwards by at most 5% while the negative ions are contracted by an order of magnitude less. This result has been supported by low-energy electron diffraction (LEED) experiments,<sup>64</sup> which, however, are not exclusively sensitive to the surface structure. Moreover, according to Engel and Rieder<sup>65</sup> these experiments may not be reliable as the electron beam gives rise to a decomposition of the surface. Unfortunately, He-atom diffraction studies are not sufficiently well developed to measure the surface puckering with the necessary precision. The theoretical models of Benedek<sup>8,9</sup> and de Wette<sup>6,7</sup> and co-workers do not ordinarily include relaxation. Chen and de Wette<sup>66</sup> have made simplified model calculations in which they have included the structural effect of relaxation. The result of these studies is that relaxation has a significant effect on the frequencies of surface phonons. Recently Tasker has carried out a lattice-dynamical calculation of the Rayleigh surface mode for a relaxed rumpled surface.<sup>67</sup> The effect of relaxation was to increase the frequency at the  $\bar{M}$  point by about 4%. He checked his shell-model potential against the transverse-acoustical bulk mode for which he got good agreement. Thus relaxation does not appear to be able to explain the discrepancy.

Another possible explanation is that the forces at the surface are different than in the bulk. Model calculations performed by Rieder<sup>68</sup> in 1970 indicated that a change in force constant at the surface could lead to a drastic lowering in the Rayleigh-mode frequency near the Brillouin-zone boundary without an appreciable effect on the bulk-projected surface frequencies. Benedek and Galimberti<sup>45</sup> have studied the effect of different polarizabilities on the surface-mode frequencies. Benedek and Garcia<sup>62</sup> have studied this for the case of LiF where because of the increased volume (greater Watson radius) available to the surface F atom, its polarizability may change substantially from the bulk value of 0.91 to 1.4 Å<sup>3</sup>. Lakshmi and de Wette<sup>69</sup> have also pointed out that charge transfer at the surface may

TABLE III. Least-squares fit to experimental dispersion curves.

Crystal	$B_1$	$B_3$	$B_5$
LiF	36.7253	2.0634	-0.1591
NaF	25.2717	0.1278	0.3809
KCl	10.9902	-0.0135	0.1315

be different than in the bulk and will tend to lower the forces and the vibrational frequencies.

More recently, Benedek<sup>70,71</sup> has suggested that the discrepancy can be understood quantitatively in the following way. First we note that at the zone boundary for an acoustical mode only the heavy F ions are vibrating, while the Li ions are stationary.<sup>71</sup> To a good approximation the frequency at the zone boundary is given by

$$\omega_{\text{RW}}^2(\bar{M}) \simeq \frac{f_s}{\mu_s}, \quad (11)$$

where  $f_s$  is the effective force constant and  $\mu_s$  is the effective mass which is close to the mass of the F ion. Thus the discrepancy can be directly related to the difference in the force constant at the surface compared to the bulk force constant  $f_b$ , which was used in the previous calculations. According to the theory of Benedek and Nardelli<sup>72</sup> an effective short-range force constant as a function of interatomic distance  $r$  can be derived for either the deformed-dipole or breathing-shell models,

$$f_s = f_{\text{RIM}} - \frac{4\pi Z^{*2}}{3r} \frac{4\pi\alpha/3r^2}{1+(4\pi\alpha/3r^2)}, \quad (12)$$

where  $f_{\text{RIM}}$  is the force constant for the Kellerman rigid-ion model,  $Z^*$  is the Sziget charge, and  $\alpha$  is the fluorine polarizability. Thus, if there is additional dynamic charge transfer, which according to de Wette<sup>73</sup> may occur at the LiF surface, then  $Z^*$  will be increased and  $f_s < f_b$ . This is related to the previously mentioned explanation by Benedek and Garcia<sup>62</sup> of an increased polarizability  $\alpha_s > \alpha_b$  which will have the same effect. Based on these guidelines Benedek and co-workers<sup>60,61</sup> have carried out an extensive series of breathing-shell calculations. The surface dispersion curve corresponding to the best fit of all the available experiments, including the neutron data, is shown in Fig. 17. In this calculation relaxation was not included and the static fluorine charge was  $Z=0.9$  to take account of the net (static) charge transfer which is also the same in the bulk and at the surface, and  $\alpha_s = 0.82 \times 10^{-24} \text{ cm}^3$  compared to the bulk value of  $\alpha_b = 0.70 \times 10^{-24} \text{ cm}^3$ .<sup>39,60,61</sup>

Thus the He-beam data have already contributed to a further refinement of crystal dynamic models and made it possible to extend them to surfaces. According to Eq. (12) the good agreement found with the original theory of NaF, KCl suggests that here the effect of relaxation may entirely compensate for the increased polarizability. To test this we

have recently carried out similar measurements for NaCl (Ref. 74) which should be more similar to LiF than NaF and KCl. No deviation from the theoretical calculations was found however.

Prior to these experiments there was considerable controversy over the relative contributions to the energy transfer with true surface modes as compared with bulk modes at the surface. The experiments show clearly that (at least for alkali halides) surface phonons are dominant. Bulk-phonon processes generally appear as featureless plateaus or tails near the Rayleigh peaks but may show some structure, as near the  $(\bar{1}\bar{1})$  peak for LiF(001) along the  $\langle 100 \rangle$  direction, which is presumably due to structure in bulk-band density of states. Careful examination of the TOF spectra<sup>47,75</sup> suggests that the sharp peaks may well be superimposed on a broad continuum presumably due to a multiphonon interaction with low-frequency bulk or surface modes. That multiphonon effects can be important is particularly apparent in the KCl spectra. The KCl spectra demonstrate, furthermore, that sharp phonon peaks can also be resolved even for soft crystals where according to the Weare criterion<sup>58</sup> single-phonon events are expected to be unlikely. The observation of sharp peaks despite the presence of multiphonon processes was recently predicted by Meyer in a theoretical study.<sup>57</sup>

Finally these experiments have shown that inelastic phonon interactions are strongly affected by selective adsorption processes. More recent work<sup>77</sup> has shown that selective adsorption has an even stronger effect on the inelastic probabilities at grazing angles. On the other hand, the process of kinematic focusing which was previously invoked to explain a structured enhancement in intensity between diffraction peaks observed in Ne-LiF scattering<sup>52</sup> could, with the present apparatus, only be clearly observed for NaF, but not for LiF and KCl.

#### ACKNOWLEDGMENTS

The authors gratefully acknowledge many fruitful discussions with G. Benedek, N. Garcia, and F. de Wette. We also wish to thank E. Hulpke and B. Feuerbacher for much sage advice and an ongoing interest in the experimental work and D. Eichenauer for carefully reading the manuscript. One of us (B.D.) thanks the Deutscher Akademischer Austauschdienst for financial support during the course of much of this work.

- \*Present address: Bell Laboratories, 600 Mountain Ave., Murray Hill, NJ 07974.
- <sup>1</sup>A. A. Maradudin, E. W. Montroll, G. H. Weiss, and I. P. Ipatova, *Theory of Lattice Dynamics in the Harmonic Approximation*, 2nd ed. (Academic, New York, 1971), Chap. IX, pp. 520–634.
  - <sup>2</sup>A. F. Devonshire, Proc. R. Soc. London Ser. A **158**, 269 (1937).
  - <sup>3</sup>C. Strachan, Proc. R. Soc. London Ser. A **158**, 591 (1937).
  - <sup>4</sup>F. O. Goodman, CRC Crit. Rev. Solid State Mater. Sci. **7**, 33 (1977).
  - <sup>5</sup>J. P. Toennies, in *Dynamics of Gas Surface Interactions* Vol. 21 of *Springer Series in Chemical Physics*, **2**, edited by G. Benedek and U. Valbusa (Springer, Berlin, 1982), pp. 208–226.
  - <sup>6</sup>R. E. Allen, G. P. Alldredge, and F. W. de Wette, Phys. Rev. B **4**, 1648 (1971).
  - <sup>7</sup>T. S. Chen, F. W. de Wette, and G. P. Alldredge, Phys. Rev. B **15**, 1167 (1977).
  - <sup>8</sup>G. Benedek, Phys. Status Solidi B **58**, 661 (1973).
  - <sup>9</sup>G. Benedek, Surf. Sci. **61**, 603 (1976).
  - <sup>10</sup>D. Castiel, L. Dobrzynski, and D. Spanjaard, Surf. Sci. **59**, 252 (1976).
  - <sup>11</sup>J. E. Black, Surf. Sci. **100**, 555 (1980).
  - <sup>12</sup>J. E. Black, B. Laks, and D. L. Mills, Phys. Rev. B **22**, 1818 (1980).
  - <sup>13</sup>J. E. Black, D. A. Campbell, and R. F. Wallis, Surf. Sci. **105**, 629 (1981).
  - <sup>14</sup>V. Bortolani, F. Nizzoli, and G. Santoro, Phys. Rev. Lett. **41**, 39 (1978).
  - <sup>15</sup>K. H. Rieder, Surf. Sci. **26**, 637 (1971).
  - <sup>16</sup>J. G. Dash and J. Ruvalds, *Phase Transitions in Surface Films* (Plenum, New York, 1980).
  - <sup>17</sup>J. W. White, R. K. Thomas, T. Trewern, I. Marlow, and G. Bromchil, Surf. Sci. **76**, 13 (1978).
  - <sup>18</sup>J. R. Sandercock, Solid State Commun. **26**, 547 (1978).
  - <sup>19</sup>S. Mishra and R. Bray, Phys. Rev. Lett. **39**, 222 (1977).
  - <sup>20</sup>H. Ibach, Phys. Rev. Lett. **24**, 1416 (1970).
  - <sup>21</sup>B. R. Williams, J. Chem. Phys. **55**, 3220 (1971).
  - <sup>22</sup>B. F. Mason and B. R. Williams, J. Chem. Phys. **61**, 2765 (1974).
  - <sup>23</sup>D. R. Miller and J. M. Horne, in *Proceedings of the Third International Conference on Solid Surfaces, Vienna, 1977*, edited by R. Dobrozemsky (Berger, Vienna, 1977), pp. 1385–1388.
  - <sup>24</sup>P. Cantini, R. Tatarek, and G. P. Felcher, Surf. Sci. **63**, 104 (1977).
  - <sup>25</sup>P. Cantini and R. Tatarek, Phys. Rev. B **23**, 3030 (1981).
  - <sup>26</sup>J. R. Bledsoe and S. S. Fisher, Surf. Sci. **46**, 129 (1974).
  - <sup>27</sup>J. M. Horne and D. R. Miller, Phys. Rev. Lett. **41**, 511 (1978).
  - <sup>28</sup>B. Feuerbacher, M. A. Adriaens, and H. Thuis, Surf. Sci. **94**, L171 (1980).
  - <sup>29</sup>B. F. Mason and B. R. Williams, Phys. Rev. Lett. **46**, 1138 (1981).
  - <sup>30</sup>G. Brusdeylins, R. B. Doak, and J. P. Toennies, Phys. Rev. Lett. **44**, 1417 (1980).
  - <sup>31</sup>G. Brusdeylins, R. B. Doak, and J. P. Toennies, Phys. Rev. Lett. **46**, 437 (1981).
  - <sup>32</sup>R. B. Doak and J. P. Toennies, Surf. Sci. **117**, 1 (1982).
  - <sup>33</sup>G. Benedek, G. Brusdeylins, R. B. Doak, and J. P. Toennies, in *Proceedings of the International Conference on Phonon Physics, Bloomington, Indiana, 1981*, edited by W. E. Bron [J. Phys. (Paris) Colloq. **42**, Suppl. 12, C6-793 (1981)].
  - <sup>34</sup>G. Brusdeylins, R. D. Doak, and J. P. Toennies, J. Chem. Phys. **75**, 1784 (1981).
  - <sup>35</sup>J. T. Lewis, A. Lehoczký, and C. V. Briscoe, Phys. Rev. **161**, 877 (1967).
  - <sup>36</sup>G. Armand, J. Lapujoulade, and Y. Lejay, Surf. Sci. **63**, 143 (1977).
  - <sup>37</sup>H. Hoinkes, H. Nahr, and H. Wilsch, Surf. Sci. **33**, 516 (1972).
  - <sup>38</sup>S. V. Krishnaswamy, G. Derry, D. Wesner, T. J. O'Gorman, and D. R. Frankl, Surf. Sci. **77**, 493 (1978).
  - <sup>39</sup>H. Wilsch, H.-U. Finzel, H. Frank, H. Hoinkes, and H. Nahr, in *Proceedings of the Second International Conference on Solid Surfaces, Kyoto, 1974, Japan* [J. Appl. Phys. Suppl. **2**, Pt. 2, 567 (1974)].
  - <sup>40</sup>B. Wood, B. F. Mason, and B. R. Williams, J. Chem. Phys. **61**, 1435 (1974).
  - <sup>41</sup>H. Frank, H. Hoinkes, and H. Wilsch, Surf. Sci. **63**, 121 (1977).
  - <sup>42</sup>S. Hart, Brit. J. Appl. Phys. (J. Phys. D), Ser. 2, **1**, 1277 (1968).
  - <sup>43</sup>G. W. Farnell, in *Physical Acoustics 6*, edited by W. P. Mason and R. N. Thurston (Academic, New York, 1970), pp. 109–166.
  - <sup>44</sup>D. C. Gazis, R. Herman, and R. F. Wallis, Phys. Rev. **119**, 533 (1960).
  - <sup>45</sup>G. Benedek and F. Galimberti, Surf. Sci. **71**, 87 (1978).
  - <sup>46</sup>G. Benedek, S. Boffi, G. Caglioti, and J. C. Bilello, Surf. Sci. **48**, 561 (1975).
  - <sup>47</sup>R. B. Doak, Ph. D. dissertation, Massachusetts Institute of Technology, 1981 (unpublished); Max-Planck-Institut für Strömungsforschung, Göttingen, Bericht 14 (unpublished).
  - <sup>48</sup>G. Brusdeylins, H.-D. Meyer, J. P. Toennies, and K. Winkelmann, in *Progress in Astronautics and Aeronautics 51*, edited by J. L. Potter (AIAA, New York, 1977), pp. 1047–1059.
  - <sup>49</sup>J. P. Toennies and K. Winkelmann, J. Chem. Phys. **66**, 3965 (1977).
  - <sup>50</sup>Dr. Karl Korth, Monokristalle—OHG, Am Jägersberg 9, 2300 Kiel 17, Federal Republic of Germany.
  - <sup>51</sup>J. Estel, H. Hoinkes, H. Kaarman, H. Nahr, and H. Wilsch, Surf. Sci. **54**, 393 (1976).
  - <sup>52</sup>G. Benedek, Phys. Rev. Lett. **35**, 234 (1975).
  - <sup>53</sup>G. Boato, P. Cantini, and L. Mattera, Surf. Sci. **55**, 141 (1976).
  - <sup>54</sup>V. Celli, N. Garcia, and J. Hutchison, Surf. Sci. **87**, 112 (1979).
  - <sup>55</sup>G. Benedek, G. Brusdeylins, R. D. Doak, and J. P. Toennies, Phys. Rev. B **27**, 2488 (1983).
  - <sup>56</sup>K. Dransfeld and E. Salzmänn, *Physical Acoustics 7*

- (Academic, New York 1970), pp. 219–272. See pp. 253–255. We are grateful to Professor Dransfeld for calling our attention to this reference and for discussing how to estimate phonon lifetimes.
- <sup>57</sup>H.-D. Meyer, *Surf. Sci.* **104**, 117 (1981).
- <sup>58</sup>J. H. Weare, *J. Chem. Phys.* **61**, 2900 (1974).
- <sup>59</sup>W. Allison, R. F. Willis, and M. Cardillo, *Phys. Rev. B* **23**, 6824 (1981).
- <sup>60</sup>G. Benedek and L. Miglio, in *Ab Initio Calculations of Phonon Spectra*, edited by J. Devreese, V. E. van Doren, and P. E. van Camp (Plenum, New York 1982), p. 215.
- <sup>61</sup>G. Benedek, G. P. Brivio, L. Miglio, and V. R. Velasco, *Phys. Rev. B* **26**, 497 (1982).
- <sup>62</sup>G. Benedek and N. Garcia, *Surf. Sci.* **103**, L143 (1981).
- <sup>63</sup>G. C. Benson and T. A. Claxton, *J. Chem. Phys.* **48**, 1356 (1968).
- <sup>64</sup>G. E. Laramore and A. C. Switendick, *Phys. Rev. B* **7**, 3615 (1973).
- <sup>65</sup>T. Engel and K. H. Rieder, *Springer Tracts in Modern Physics* (Springer, Berlin, 1982), Vol. 91, pp. 55–180.
- <sup>66</sup>T. S. Chen and F. W. de Wette, *Surf. Sci.* **74**, 373 (1978).
- <sup>67</sup>P. W. Tasker, J. Hoare, and P. Masri, private communication. See also P. W. Tasker, *Solid State Ionics* (in press).
- <sup>68</sup>S. W. Musser and K. H. Rieder, *Phys. Rev. B* **2**, 3034 (1970).
- <sup>69</sup>G. Lakshmi and F. W. de Wette, *Phys. Rev. B* **22**, 5009 (1980).
- <sup>70</sup>G. Benedek, private communication.
- <sup>71</sup>J. P. Toennies, *Phys. Scr.* **T1**, 89 (1982).
- <sup>72</sup>G. Benedek and G. F. Nardelli, *J. Chem. Phys.* **48**, 5242 (1968).
- <sup>73</sup>F. de Wette, private communication.
- <sup>74</sup>G. Benedek, G. Brusdeylins, R. B. Doak, J. G. Skofronick, and J. P. Toennies (unpublished).
- <sup>75</sup>G. Benedek, R. B. Doak, and J. P. Toennies (unpublished).
- <sup>76</sup>G. Lilienkamp and J. P. Toennies, *Phys. Rev. B* **26**, 4752 (1982).
- <sup>77</sup>G. Lilienkamp and J. P. Toennies, *J. Chem. Phys.* (in press).